1-Butanol Production from the Ethanol Producing Industry Wastes Using Cu-Ni-Mn-Nanocomposites

DELİA TERESA SPONZA, RUKİYE ÖZTEKİN *
[a] Department of Environmental Engineering
Dokuz Eylül University
Tınaztepe Campus, 35160 Buca/Izmir,
TURKEY

**Corresponding Author*

Abstract: - Ethanol (C_2H_5OH or EtOH) has lower energy content, adsorbs water and leads to separation and dilution problems in storage tanks and is corrosive to fuel infrastructure. 1-butanol (C_4H_9OH or 1-BuOH) have fuel properties and is more closely resemble those of gasoline. Therefore, becoming a promising alternative to ethanol as a substitute for fossil fuels, it is essentially non-corrosive, and has an energy density of 90%. Therefore, in this study, it was aimed to produce 1-butanol from the ethanol wastes using copper-nickel-manganese nanocomposites (Cu-Ni-Mn-NCs). Nano Cu and nano-Ni were hydrogenating/dehydrogenating components and manganese oxide (MnO_2) has acid/base properties and provides high surface area. The catalysts were characterized by X-ray diffraction (XRD), temperature-programmed reduction (TPR), specific surface area, ammonia (NH_3) temperature-programmed desorption (TPD), carbon dioxide (CO_2) chemisorption, transmission electron microscopy (TEM), energy-dispersive X-ray spectroscopy (EDX), and X-ray photoelectron spectroscopy (XPS) analyses, respectively. XRD, TEM, XPS analysis showed nanocomposite production followed a Guerbet route and demonstrated good stability and activity. The effects of Cu-Ni-Mn NCs concentrations and pH levels on the production of 1-butanol was studied. The maximum 1-butanol production yield was 96% at an ethanol concentration of 4 mg/l at 2 mg/l Cu-Ni-Mn NCs concentration at a Mn percentage of 18% after 15 min at a pH of 8.02. Cu-Ni-Mn NCs can be used for 1-butanol production from the ethanol producing industry wastes.

Key-Words: - Aldol condensation; 1-Butanol (C_4H_9OH or 1-BuOH); Cu-Ni-Mn-Nanocomposite; Dehydrogenation; Energy production; Ethanol (C_2H_5OH or EtOH) condensation; Fuel; Guerbet reaction; Hydrogenation; OXO (Hydroformylation) process.

Received: August 14, 2025. Revised: November 22, 2025. Accepted: December 18, 2025. Published: March 20, 2026.

1 Introduction

Interest in biofuels has increased considerably over recent years, particularly in view of concerns over climate change and energy security, [1]. One of the most common bio-fuels is ethanol which can be used as an additive to gasoline in unmodified gasoline engines, [2], or in high concentrations in more specialist engines. However, ethanol has a number of problems as a fuel, including its miscibility with water, corrosion, and low energy content per unit volume compared to gasoline.

Therefore, 1-butanol has advantages as a fuel, because it has a higher energy content than ethanol, lower water absorption and better miscibility with gasoline. Current gasoline engines need little or no modification to burn neat 1-butanol, [2]. Furthermore, unlike ethanol, butanol can be transported without major problems in current gasoline pipelines. Industrially, 1-butanol is manufactured *via* the high-pressure OXO process (Hydroformylation process), [2], where propylene is hydroformylated to butyraldehyde using syngas and a homogeneous rhodium catalyst; butyraldehyde is subsequently hydrogenated to butanol. Alternatively, 1-butanol can be produced from acetaldehyde *via* an aldol condensation, again followed by hydrogenation, [3].

Bioethanol, obtained by fermentation of different biomass materials and wastes, has dominated so far, the bio-based feedstock market, used by itself or as a mixture with conventional fuels. However, ethanol has a number of significant drawbacks compared to

gasoline: it has lower energy content, adsorbs water, leads to separation and dilution problems in storage tanks and is corrosive to the current technology of engines and fuel infrastructure, [4]. In contrast, 1-butanol have fuel properties that more closely resemble those of gasoline, becoming a promising alternative to ethanol as a substitute for fossil fuels, as it is essentially non-corrosive, immiscible with water and has an energy density of 90%, [5].

The interest in the production of 1-butanol has grown nowadays also due to its application as a raw material in the manufacture of chemical products in the paint and solvent industry, which include the production of butyl acetate, butyl acrylate, glycol ethers, resins and plasticizers, [4], [5], [6]. Traditionally, 1-butanol has been produced by the fermentation of sugars (ABE process) or through the petrochemical oxo process. In the ABE process, bacterial fermentation gives place to a mixture of acetone, butanol and ethanol, which is then subjected to a separation procedure. This process was developed in 1920, although, it became non-profitable due to the lack of competitiveness with the OXO process, [7]. In this latter method, propylene reacts with syngas [mixture of carbon monoxide (CO) and hydrogen (H_2)] forming butyraldehyde which is subsequently hydrogenated to produce butanol, [8]. Therefore, the use of fossil fuels derivatives as raw materials and its high cost have made this process less attractive in the recent years, when ‘’green’’ processes and renewable materials are more desirable. The direct condensation of ethanol into 1-butanol is considered a more desirable route, since the reaction is faster when compared to the ABE process and fewer steps are necessary to get to the product.

1-butanol can also be produced from ethanol *via* a sequence of steps collectively known as the Guerbet reaction. 1-butanol is produced by ethanol condensation, which implies dehydrogenation of ethanol to acetaldehyde, aldol condensation of acetaldehyde to crotonaldehyde and hydrogenation of crotonaldehyde to 1-butanol, [9], (Fig. 1). Guerbet industrial process employs homogeneous catalysts, although, recent research focuses on its heterogenization. While the ethanol dehydrogenation to acetaldehyde, as well as the hydrogenation of reaction intermediates to 1-butanol require easily heterogenizable metal catalysts, the aldol condensation step is more difficult to perform on solid metal oxides. Several heterogeneous systems have been reported for this reaction, the majority associated to basic or acid/base properties like metal-Mg-Al mixed oxides, hydroxyapatites, group II metal oxides like magnesium oxide (MgO), sodium (Na) modified zirconia (ZrO_2) and hydrotalcite based catalysts, among others, usually employing reaction temperatures over 300ºC, [6], [8], [10], [11], [12], [13], [14], [15].

* Figure 1 can be found in the Appendix section.

Koda et al., [16], have used a homogeneous iridium (Ir) catalyst in the presence of 1,7-octadiene and ethanol sodium ethoxide (EtONa) to promote the Guerbet reaction achieving turn over numbers (TONs) in excess of 1200 with 51% selectivity towards 1-butanol at 38% ethanol conversion. Recently they reported a range of ruthenium centred catalysts, [15]. In their system, a selectivity towards 1-butanol of 94% was achieved, but the conversion was only a little over 20%, with TONs only in the hundreds, [15]. The Guerbet reaction has also been demonstrated successfully in batch processes for a variety of different heterogeneous systems, including Lithium (Li)-exchanged Zeolites, [14], MgO, [11], Magnesium/aluminium (Mg/Al) mixed metal oxides, [17], and hydroxyapatites, [8], [18]. Many of these systems, however, suffer from poor conversions or selectivity and require temperatures above 400°C and long reaction times, [19].

Copper (Cu) and nickel (Ni) have been studied as a metallic component to catalyse the Guerbet reaction since its presence considerably speed up the hydrogenation/dehydrogenation steps and consequently reduces the reaction temperature, [5], [20], [21], [22], [23]. Moreover, combined use of both metals is reported to increase 1-butanol selectivity, [24], [25]. In order to improve the catalytic activity, an inert and non-porous carbonaceous support, high surface area graphite (HSAG), has been used in the study to disperse the active phases (manganese oxide, MnO and reduced metallic precursors) maximizing the number of surface centers exposed and favouring their interaction, [26], [27]. In particular, their advantageous properties make carbon supports the most suitable material for the coupling of ethanol since they are reported to increase the strength of basic sites when metal oxides are dispersed over them and the hydrophobic nature of HSAG could play a key role as water molecules are produced as a by-product, [28], [29].

Manganese (Mn) based catalysts have not been extensively studied for the condensation of ethanol into 1-butanol, being most of these studies homogeneous catalysed in presence of a base and only a few studies have been of heterogeneous catalysis, [14], [30], [31], [32]. Among the heterogeneous catalysed studies found in literature, Ghaziaskar et al., [30], performed the condensation of ethanol with a mixed oxide of Mn_2O_3 and Ni supported over Al in a fixed-bed reactor reaching 64% of 1-butanol selectivity with an ethanol conversion of 18.70% at 250ºC. Marcu et al., [14], performed this reaction in an autoclave at 200ºC with MMgAlO mixed oxide catalysts [M=lead (Pd), silver (Ag), Mn, iron (Fe), Cu, samarium (Sm), Ytterbium (Yb)]. Concretely over Mn-Mg-AlO mixed oxide a 1-

butanol selectivity of 53.30% was reached but with a very low conversion. The surface basicity of the catalysts which showed that this latter catalyst presented mostly medium and high strength base sites. Therefore, the presence of high strength basic sites is required to obtain higher selectivity towards n-butanol. MnO seems a suitable material for the Guerbet reaction since it has been reported to improve the activity of the dehydrogenation step to acetaldehyde resulting in an increased ethanol conversion at temperatures about 300°C–400°C, [33], [34], [35], [36].

Since the ethanol dehydrogenation to form acetaldehyde is commonly considered as a limiting step of the Guerbet process, the incorporation of metals to the catalytic system is implemented to reduce the high reaction temperatures necessary to overcome this step. Bearing this in mind, Cu and Ni have been studied as a metallic component to catalyse the Guerbet reaction since its presence considerably speed up the hydrogenation/dehydrogenation steps and consequently reduces the reaction temperature, [5], [20], [21], [22], [23]. Moreover, combined use of both metals is reported to increase 1 butanol selectivity, [24], [25]. In order to improve the catalytic activity, an inert and non-porous carbonaceous support, HSAG, has been used in this study to disperse the active phases (manganese oxide and reduced metallic precursors) maximizing the number of surface centers exposed and favouring their interaction, [27], [26]. In particular, their advantageous properties make carbon supports the most suitable material for the coupling of ethanol since they are reported to increase the strength of basic sites when metal oxides are dispersed over them and the hydrophobic nature of HSAG could play a key role as water molecules are produced as a by-product, [28], [29].

In this study, it was aimed to produce 1-butanol from the ethanol wastes using Cu-Ni-Mn NCs. Nano-Cu and nano-Ni were hydrogenating/dehydrogenating components and MnO has acid/base properties and provides high surface area. The catalysts were characterized by XRD, TPR, specific surface area, NH_3 temperature-programmed desorption, CO_2 chemisorption, TEM, EDX and XPS analyses. XRD, TEM and XPS analyses showed nanocomposite production followed a Guerbet route and demonstrated good stability a remaining active. The effects of Cu-Ni-Mn-NCs concentrations and pH levels on the production of 1-butanol was studied. ANOVA statistical analysis was calculated for all samples.

2 Material and Methods

2.1 Materials

Ethanol (Dehydrated) was purchased from Biosolve BV, The Netherlands. 1-propanol (99%), 1 butanol (99%), 1-pentanol (99%), 1-hexanol (99%) were purchased from TCI EUROPE N.V. Tetrahydrofuran (THF) (99.5%) was purchased from Boom BV. $AlCl_3.6H_2O$ (≥ 98%), $MgCl_2.6H_2O$ (≥ 99%), $Ni(NO_3)_2.6H_2O$ (> 99%) were purchased from Alfa Aesar. $Cu(NO_3)_2.2.5H_2O$ (98%), Decane (≥ 99.0%) were purchased from Sigma Aldrich. All chemicals were used as received without further purification.

2.2 Leaching Test

After reaction, the liquid sample as well as the catalyst was quantitatively transferred to a 50 ml centrifuge tube. Additional THF was used to wash the reactor and recover all catalyst residues (up to 10 ml total volume). After centrifugation, 1 ml of the solution was transferred to a glass vial and evaporates all the liquid using rotary evaporator. Then, 7 ml HNO_3 was added to dissolve all the metal and analysed by Perkin Elmer instrument (Optima 7000DV).

2.3 Recycling Test

After a typical catalytic run (0.1 g $Cu_{10}Ni_{10}$-PMO, 3 ml ethanol, 310°C, 6 h), the catalyst was separated from the reaction solution by centrifugation and subsequent decantation. The solid was additionally washed with THF (2 × 10 ml), then with acetone (1 × 10 ml), and dried overnight at room temperature (at 25°C) under vacuum prior to the next run.

2.4 Catalyst Preparation

The HTC (hydrotalcite) catalyst precursors were prepared by a coprecipitation method, according to literature procedures, [37], [38]. In a typical procedure, a solution containing $Mn(NO_3)_2$ (0.06 mol, 12.2 g) $AlCl_3.6H_2O$ (0.025 mol, 6.0 g), $Cu(NO_3)_2 \cdot 2.5H_2O$ (0.0075 mol, 1.74 g), and $Ni(NO_3)2.6H_2O$ (0.0075 mol, 2.18 g) in deionized water (0.10 l) was slowly added to an aqueous solution (0.15 l) of Na_2CO_3 (0.025 mol, 1 g) at 60°C under vigorous stirring. The pH was carefully maintained between 9.0 and 10.0 by adjusting with frequent additions of an aqueous solution of sodium hydroxide (NaOH) (1 M). The mixture was vigorously stirred for 72 h at 60°C. After cooling to room temperature (at 25°C), the suspension was filtered, and the solid was washed with deionized water and resuspended into a solution of Na_2CO_3 (2 M) which was stirred for 24 h at 40°C. After the catalyst precursor was filtered, it was washed with deionized water until the washings were chloride-free. The solid was dried at 120°C overnight, and the HTC precursor was obtained as blue powder (6.68 g). The corresponding Cu−Ni-doped porous metal oxide ($Cu_{10}Ni_{10}$-PMO) was obtained after calcining the HTC material at 460°C for 24 h in air.

2.5 Catalysts Synthesis

2.5.1 Deposition of MnO_2 Nanoparticles (NPs) on the Support

A high surface area graphite (HSAG) supplied by Timcal (S_{BET}=396 m^2/g) was used as catalyst support. The Mn/HSAG sample was prepared by wetness impregnation method with an aqueous solution containing the necessary quantity of $Mn(NO_3)_2$ precursor ($Mn(NO_3)_2 \cdot 4H_2O$, Panreac) to achieve an atomic proportion Me (Cu or Ni)/Mn 2 / 1. After that, the resulting material was dried overnight at 110ºC and then treated at 400ºC for 3 h in a quartz tube reactor under Helium gas [He(g)] atmosphere with a heating rate of - 268ºC/min.

2.5.2 Deposition of Metallic Nanoparticles on the Support

Catalysts 5Cu/HSAG, 5Ni/HSAG, 2.5Cu2.5Ni/HSAG, 5Cu-Mn/ HSAG, 5Ni-Mn/HSAG, 4Cu1Ni-Mn/HSAG and 2.5Cu2.5Ni-Mn/HSAG were prepared by wetness impregnation with aqueous solutions of the corresponding metal nitrate ($Cu(NO_3)_2.3H_2O$, Sigma-Aldrich, and $Ni(NO_3)_2.6H_2O$, Alfa Aesar) with the adequate concentration to incorporate a loading of 5 wt% metal on HSAG or Mn/HSAG: 5 wt.%Cu; 5 wt.% Ni; 4 wt.% Cu and 1 wt.% Ni; and 2.5 wt.% Cu and 2.5 wt.% Ni for each case. The resulting materials were air-dried at 110ºC overnight. Finally, the samples were treated for 1 h under flowing hydrogen (H_2) (20 ml STP/min) at 300ºC, except Ni/HSAG and Ni-Mn/HSAG which were reduced at 450ºC. The reduction temperatures of each sample were set as a result of the TPR profiles.

2.6 Modeling and Simulation of Reactors in Plug Flow Reactor (PFR) and Packed Bed Reactor (PBR) Series for the Conversion of Methanol into 1-Butanol

The parameters related to the geometry and operation of series reactors in continuous mode, in particular the plug flow reactor and the packed bed reactor (fixed bed reactor), were simulated to obtain the best dimensions and optimize the process from the degree of conversion of methanol.

2.6.1 Mathematical Model Material and Thermal Balance of the PBR

Mathematical model material and thermal balance of the PBR (Eq. 1):

$$dQ = U(T_S - T)dA_p = \frac{4U}{D}(T_S - T)dV_r \quad (1)$$

The following assumptions were made for the development of the dimensioning for which the PFR performance of the reaction rate equations is of the first order (Fig. 2).

* Figure 2 can be found in the Appendix section.

The various pre-requisites are such that: i) the reactor operates in a state of equilibrium ii) the reaction is in the liquid phase with constant density, and iii) the pressure drop along the reactor is negligible, [39].

2.6.2 Modeling of PFR and PBR Reactors in Series and Calculation of Parameters

Considering the above relation, the equation giving the volume of the PFR is as follows, [40], in Eq. (2), Eq. (3) and Eq. (4):

$$V_R = C_{A0} V_0 \int_0^{X_{AF}} \frac{dX_A}{-r_A} \quad (2)$$

$$\frac{V_R}{V_0} = C_{A0} \int_0^{X_{AF}} \frac{dX_A}{-r_A} \quad (3)$$

$$\tau = C_{A0} \int_0^{X_{AF}} \frac{dX_A}{-r_A} \quad (4)$$

After adjusting the material balance from the differential elements to give an expression for the volume of the reactor, we have as follows, [39], in Eq. (5), Eq. (6) and Eq. (7):

$$V_R = F_{A0} \int_0^{X_{AF}} \frac{dX_A}{-r_A} \quad (5)$$

$$C_A = \frac{P}{RT} \quad (6)$$

$$-r_A = kC_A^2 \quad (7)$$

2.6.3 Development of the Dimensioning of the PBR

Firstly, for a heterogeneous reaction (e.g fluid-solid), the mass of the solid catalyst, *W*, is a bigger problem than that of determining the volume of the reactor, [41]. Thus, for the Packed Bed Reactor (PBR), if the pressure drop and the degradation of the catalyst are neglected for this purpose, its model will have been established, [41], in Eq. (8), Eq. (9) and Eq. (10):

$$W_{cat} = \frac{F_{A0} \int_0^x x_A}{-r_{oxy}} \quad (8)$$

Where, *W*, is the mass of the catalyst required to reduce the molar feed rate of *A*, F_{A0} for a conversion x_A.

$$V_{cat} = \frac{W_{cat}}{\rho_{cat}} \quad (9)$$

$$-r_{oxy} = x_A \frac{WHSV}{Mm_A} \cdot \left(\frac{1h}{3600s}\right) \quad (10)$$

Knowing the residence time, the volume of the reactor is deduced by the following relation in Eq. (11) and Eq. (12):

$$V_{PBR} = \tau \, x \, V_0 \quad (11)$$

$$V_0 = F_A \, x \, V_m \quad (12)$$

Thus, the volume of the reactor depends only on the feed rate.

2.7 Calculation of the Reaction Rate (kinetic Analysis), Material Balance, Residence Time, and PFR Volume

Methoxymethane can be produced by the following reaction kinetics (Table 1) and in Eq. (13) and Eq. (14):

$$2CH_3OH \leftrightarrow CH_3OCH_3 + H_2O \quad (13)$$

$$-r_A = k_0 e^{\left[\frac{-E_0}{RT}\right]} C_A \quad (14)$$

* Table 1 can be found in the Appendix section.

2.8 Catalysts Characterization

2.8.1 XRD Analysis

Structural properties of the catalysts were determined by X-ray diffraction (XRD), using Polycristal X'Pert Pro PANalytical diffractometer operating with Cu Kα radiation (λ =1.54 Å, 45 kV and 40 mA) and a Ni filter. Data were collected in the 2θ range between 4° and 90° at a rate of 0.04°/s. PANalytical X'Pert HighScore Plus software was used for qualitative analysis.

2.8.2 Temperature Programmed Reduction (TPR) Analysis

Temperature programmed reduction (TPR) was carried out to study the reduction behaviour of the catalysts and the interaction between the metal phases and the support. The experiments were performed in a U-shaped quartz reactor under 30 ml/min of a mixture of 4 vol.% H_2 in He(g) (Air Liquide 99.999% purity). For each TPR experiment, 150 mg of catalyst were heated from room temperature (at 25ºC) up to 700ºC with a ramp of – 263.15ºC/min. Effluents were analysed by using a gas chromatograph (GC) (Varian 3400) equipped with a thermal conductivity detector (TCD) and a Porapack Q column, [42].

2.8.3 Specific Surface Area (S_{BET}) Measurements

The measurements of the specific surface area (S_{BET}) and average pore volume of the support as well as those of the catalysts were carried out using an automatic volumetric adsorption Micromeritics ASAP 2010 instrument where the nitrogen (N_2) adsorption-desorption isotherms were collected at - 196ºC. Prior to N_2 adsorption, the samples were outgassed for 5 h at 150ºC.

2.8.4 Temperature Programmed Desorption (TPD) Analysis

Catalysts surface acidity was determined by TPD of NH_3 in a flow system with thermal conductivity detector. The in situ reduced sample was previously saturated with NH_3(g) 5% at 50ºC, swept with He(g) at 100ºC and then heated from 100ºC to 350ºC at – 263ºC/min.

2.8.5 CO_2 Chemisorption Analysis

The basic sites were analysed by determination of CO_2 adsorption heats using a differential heat-flow microcalorimeter of the Tian-Calvet type C80 from Seta ram coupled to a volumetric equipment described in detail in a previous work, [43]. The samples (200 mg) were pretreated for 10 h under vacuum at 350ºC and outgassed overnight. Successive doses of CO_2 were introduced into the system at 50ºC to titrate the surface of the catalysts until a final pressure of 0.009211 atm was reached. The differential heats of adsorption (Q_{diff}) were obtained as the ratio between the exothermic integrated values of each pulse and the adsorbed amount of CO_2.

2.8.6 TEM Analysis

Transmission electron microscopy (TEM) study was used to assess the particle size of metal nanoparticles (NPs) and the distribution of metal and manganese dioxide (MnO_2) phases on the support. TEM micrographs and mappings were obtained on a JEOL JEM-2100 F microscope at 200 kV and a JEM 3000 F microscope at 300 kV, both equipped with an Energy-Dispersive X-Ray (EDX) detector. The samples were ground to powder and suspended in ethanol using an ultrasonic bath before deposition over a gold grid with carbon coated layers (Aname, Lacey carbon 200 mesh) and the ethanol was evaporated at room temperature before introducing the sample in the microscope. The Scanning Transmission Electron Microscopy (STEM) was done using a spot size of 1 nm. The average diameter (d) of Cu and Ni particles was calculated based on a minimum of 300 particles, using the following equation (Eq. 15):

$$d = \frac{\sum n_i d_i^3}{\sum n_i d_i^2} \quad (15)$$

where n_i is the number of particles with diameter (d_i).

2.8.7 EDX Analysis

To investigate the morphological properties and structure of the synthesized catalyst and the composition of the elements present in the synthesized

catalyst; an EDX spectrometry instrument (TESCAN Co., Model III MIRA) was used.

2.8.8 XPS Analysis

XPS spectra were collected with a SPECS GmbH with UHV system, energy analyser PHOIBOS 150 9MCD under non-monochromatic X-ray source of Mg (200 W, 1253.6 eV). Prior to the analysis, each sample was pressed into a small pellet of 10 mm diameter, placed in the sample holder and degassed in the chamber for 24 h to achieve a dynamic vacuum below 9.9×10^{-14} atm. The spectral data for each sample were analysed using CASA XPS software. The binding energy (BE) was referenced to the C 1s peak at 284.6 eV. The equipment error in the energy determinations is less than 0.01 eV. The resulting spectra were deconvoluted and fitted to a mix of Gaussian and Lorentzian curves.

2.9 Analysis of Products

After reaction, the solids were separated by filtration and the composition of the liquid phase was analysed by GC-MS and GC-FID. Besides the main product 1-butanol, a variety of other compounds were detected, which were comprehensively analysed. Compounds with a similarity match higher than 80% based on GC-MS identification and all these compounds accounted for a total area percentage > 95% in all samples. Quantification was carried out by GC-FID with the use of calibration curves and decant as internal standard and the calibrated compounds accounted for > 90% of total products in all samples. Conversion and yield values were calculated based on the equations shown in the quantification part. The gas phase of a reaction with Cu10Ni10-PMO was analysed by GC-TCD after reaction using a 25 ml Parr reactor (reaction conditions: 10 ml ethanol and 0.30 g Cu10Ni10-PMO catalyst, 300ºC, 6h). During the reaction, the pressure increased to 80 bar at 300ºC and read 40 bar when cooling to room temperature which indicates the formation of volatile products during reaction as well. Main compounds in the gas phase included: methane (CH_4), ethylene, ethane, propane, H_2, CO, and CO_2.

2.10 Catalytic Reaction

The catalytic condensation of ethanol was carried out in a stainless-steel fixed-bed reactor operated in gas phase at 230ºC and 49.4 atm in a continuous flow. The catalysts (0.5 g) were reduced in situ with hydrogen at 300ºC for 1 h before reaction, except Ni/HSAG and Ni-Mn/HSAG, which were reduced at 450ºC. In order to study the influence of pretreatment temperature, one additional experiment was carried out with the catalyst 2.5Cu2.5Ni-Mn/HSAG, therefore it was also treated in helium at 450ºC for 1 h prior reduction with H_2. For all experiments, the feed mixture consisted of 50 ml STP/min of He(g) and 0.02 ml/min of ethanol (absolute extra pure, Scharlau) introduced with a high-pressure liquid chromatography (HPLC) pump.

The condensed reaction products were collected and analysed by gas chromatography (GC), while the gaseous products were analysed by on-line GC. The analysis of the collected products was carried out with a gas chromatograph (Bruker Scion 436) fitted with a flame ionization detector (FID) and a capillary column BR-Swax. The analysis of gaseous products was monitored with two gas chromatographs (Varian CP 3380) equipped with FID and TCD detectors and configured with a capillary column SupelQ Plot and 60/80 Carboxen-1000 column, respectively. Calibration of the possible reaction products was done with commercial standards. After 24 h of reaction time, the ethanol conversion X_{EtOH} and the selectivity to a specific product were calculated as follows, [44], (Eq. 16 and Eq. 17):

$$X_{EtOH}(\%) = \frac{\sum_i n_i mol_i}{2mol'_{EtOH} + \sum_i n_i mol_i} \; x\; 100 \qquad (16)$$

$$S_i\;(\%) = \frac{n_i mol_i}{\sum_i n_i mol_i} \; x\; 100 \qquad (17)$$

where; n_i is the number of carbon atoms of the product i, mol_i is the number of mol of the product i, and mol´ ethanol is the number of mol of unreacted ethanol.

The carbon balance ($C\%$), which resulted higher than 90%, was defined as (Eq. 18):

$$C\;(\%) = \frac{\sum_i n_i mol_i + 2mol'_{EtOH}}{2mol_{EtOH}} \; x\; 100 \qquad (18)$$

In addition, site time yield *STY (%)* of 1-butanol was defined as the number of μmol of 1-butanol produced per hour and per active site of the catalyst. The active sites were considered the total number of metal atoms on the surface M_S, which was calculated for each metal as a function of the number of metal atoms, M_t, and the metal dispersion, D (Eq. 19):

$$M_S = M_t \; x \; D \qquad (19)$$

where the metal dispersion was calculated by D (Eq. 20):

$$D = \frac{(6\; N_S \; x \; M_w)}{(\rho \; x \; N \; x \; d)} \qquad (20)$$

where ρ is the density of the metal (8.96 g/cm^3 for Cu and 8.9 g/cm^3 for Ni), Ns is the number of atoms at the surface per unit area ($1.47\cdot1019$/m^2 for Cu and $1.54\cdot1019$/m^2 for Ni), [45], M_w as the atomic weight of the element, N is Avogadro's constant and d is the average particle size (determined by TEM, assuming

that particles are spherical). Therefore, the metal dispersion for each element was calculated as (Eq. 21):

$$D = \frac{a}{d} \quad (21)$$

With a=1.04 for Cu and a=1.01 for Ni.

2.11 Guerbet Reaction Mechanisms

The Guerbet reaction for butanol synthesis from bioethanol has gained increasing attention over the years, [4], [46], [47], as butanol is regarded as a promising fuel additive. One of its key advantages is its similarity to gasoline, particularly in energy density and lower corrosiveness compared to bioethanol, which results from its reduced water affinity. This property allows butanol to be compatible with existing combustion engine technologies, [5], [9]. Given these characteristics, butanol derived from biomass has been explored as a potential precursor for the production of aviation fuels, [48]. The conversion of bioethanol to 1-butanol via the Guerbet reaction follows multiple re action steps (Fig. 3), which can be outlined as follows: (R1) ethanol dehydrogenation to form acetaldehyde, (R2) aldol condensation of acetaldehyde, yielding 3-hydroxybutanal, which can subsequently undergo dehydration to form 2-butenal (R3), followed by sequential hydrogenation reactions (R4 and R5) leading to butyraldehyde and ultimately 1-butanol, [9], [49].

* Figure 3 can be found in the Appendix section.

Since this is a multi-step transformation, several side reactions may occur. According to previous studies, common by-products include 1,1-diethoxyethane, formed through acid-catalysed acetylation of acetaldehyde with ethanol, [50], and ethyl acetate, resulting from the dehydrogenation of a hemiacetal intermediate, [47]. Additionally, diethyl ether and ethylene can be produced via acid-mediated ethanol dehydration, [45], [47]. At temperatures above 227^{o}C, 1-butanol may undergo further condensation, forming higher alcohols such as 1-hexanol and 1-octanol, [51]. Other reported by-products include CH_4, CO, acetone, propane, pentane, butane, and butene, [15], [36], [45]. Ultimately, the selection of an appropriated catalyst plays a crucial role in steering the reaction pathway toward higher 1-butanol yields, minimizing undesired side reactions.

Since aldol condensation relies on the presence of basic sites, while the dehydration of 3-hydroxybutanal requires acidic sites, an effective catalyst must incorporate both acidic and basic surface functionalities, along with metallic components to facilitate dehydrogenation/hydrogenation steps, [47], [52]. Traditionally, the industrial Guerbet process has been carried out using homogeneous catalysts, primarily alkali metal hydroxides and transition metal complexes. However, heterogeneous catalysts offer key advantages, including reusability, which enables more sustainable and environmentally friendly processes. Additionally, they contribute to minimizing waste generation and lowering energy consumption during the reaction, [51].

The development of heterogeneous catalysts for the Guerbet reaction is relatively simple when considering hydrogenation and dehydrogenation processes, as metal-based catalysts can be tailored to efficiently drive these transformations, [22]. However, incorporating both acidic and basic surface properties into solid materials, essential for aldol condensation catalysis and closely linked to the presence of metal oxides, remains a more complex challenge. In essence, the design of multifunctional catalysts must integrate both metallic sites and acidic/basic metal oxides, ensuring that basic sites selectively promote acetaldehyde condensation, acidic sites facilitate the dehydration of 3-hydroxybutanal, and metallic species enable ethanol dehydrogenation as well as hydrogenation of 2-butenal and butyraldehyde (Fig. 3). It is important to note that these active sites, located on the same solid surface, may operate synergistically during the reaction or function independently at different stages, [4], [52].

2.12 Statistical Analysis

ANOVA analysis of variance between experimental data was performed to detect F and *P* values. The ANOVA test was used to test the differences between dependent and independent groups, [53]. Comparison between the actual variation of the experimental data averages and standard deviation is expressed in terms of F ratio. F is equal (found variation of the date averages/expected variation of the date averages). *P* reports the significance level, and d.f indicates the number of degrees of freedom. Regression analysis was applied to the experimental data in order to determine the regression coefficient R^2, [54]. The aforementioned test was performed using Microsoft Excel Program.

All experiments were carried out three times and the results are given as the means of triplicate samplings. The data relevant to the individual pollutant parameters are given as the mean with standard deviation (SD) values.

3 Results and Discussions

3.1 Structural Properties

The samples 5Cu/HSAG and 5Cu-Mn/HSAG show a reduction peak at 212^{o}C and 247^{o}C, respectively, corresponding to the reduction of Cu^{+2} to Cu^{0}, [55], [56], [57]. The presence of Mn shifts the reduction of Cu at higher temperatures, suggesting close interaction

between the Cu and the MnO_2 since species harder to reduce are those with stronger interaction with metal oxides, [57], [58], [59], [60].

Additionally, catalysts 5Ni/HSAG and 5Ni-Mn/HSAG show the opposite behaviour with two reduction peaks, the first one sharper at 267ºC and the second one in the range 312ºC to 412ºC for 5Ni/HSAG, while 5Ni-Mn/HSAG shows the first peak at 252ºC and the second one in the range 322ºC to 507ºC. These TPR profiles are in accordance with others studies found with Ni supported over carbon nanotubes (CNT), [57], and HSAG, [61], [62], where the first sharp peak is due to the reduction of dispersed Ni^{+2} and the second broad one is attributed to the reduction of remaining Ni^{+2} in addition to gasification of C atoms in the vicinity of the Ni particles, which catalyse this reaction producing methane. Catalysts containing both Cu and Ni show the first sharp peak at lower temperatures the more wt% of Cu is present, meanwhile the second broad peak is smoother and almost indistinguishable for 4Cu1Ni-Mn/HSAG (Fig. 4).

* Figure 4 can be found in the Appendix section.

There is no appreciable contribution of MnO_2 reduction since the TPR profiles of samples 5Cu/HSAG, 5Ni/HSAG and 2.5Cu2.5Ni/HSAG and their counterparts with Mn are practically identical in shape, they are displaced in the X axis as a result of changes in the dispersion state when supported over Mn/HSAG. Given that $Mn(NO_3)_2$ was used as a precursor and that Mn/HSAG was treated in He(g) at 400ºC, the oxidation state expected for manganese is Mn^{+2} and therefore no reduction profile could be attributed to higher oxidation states of Mn. Bearing in mind these profiles, reduction temperature was set at 300ºC for the catalysts containing Cu and 450ºC for those containing only Ni (Fig. 4).

3.1.1 XRD Analysis Results

The X-ray diffraction patterns of the HSAG support and the resulting metal/HSAG and metal-Mn/HSAG catalysts reduced at 300ºC with H_2, except 5Ni/HSAG and 5Ni-Mn/HSAG catalysts that were reduced at 450ºC (Fig. 5). Sample 2.5Cu2.5Ni-Mn/HSAG was also studied after thermal treatment at 450ºC and reduction with H_2, even though its XRD pattern is not shown for the sake of brevity since the diffractogram is practically identical to the same sample only reduced in H_2. As can be observed in Fig. 5, no diffraction peak could be ascribed to any MnO suggesting that MnOx crystallites are either too small or in low concentration to be detected by XRD. These results are expected since all samples contain approximately 2wt% of Mn.

* Figure 5 can be found in the Appendix section.

The reflections corresponding to HSAG were detected at 2θ of 26.2, 43.9, 54.6 and 77.6° for all samples. It must be taken into account that the broad peak at 2θ=43.9° overlaps the highest distinct peaks of metallic Cu (43.5°) and Ni (44.4°). However, reflections corresponding to metallic Cu were detected in the metal-Mn/HSAG catalysts and they were only discernible in the 5Cu/HSAG and 2.5Cu2.5Ni/HSAG samples, whereas the peak of higher intensity corresponding to metallic Ni is slightly perceptible in the samples with Ni alone (5Ni/HSAG and 5Ni-Mn/HSAG), implying that the incorporation of Mn to the carbonaceous support produce bigger particle size and worse dispersion of the Cu NPs than the HSAG alone. XRD patterns of reduced 5Cu/HSAG, 5Cu-Mn/HSAG and 5Ni-Mn/HSAG catalysts suggest that these samples might have suffered a slight surface oxidation due to ambient exposition since the peaks of copper oxide (CuO) (35.7°, 38.9°) and nickel oxide (NiO) (37.4°, 43.5°) are perceptible to some extent (Fig. 5).

3.1.2 S_{BET} Measurements

The specific surface area, BET (S_{BET}) measurements were performed for the support HSAG, the sample Mn/HSAG and the M-Mn/HSAG catalysts reduced at their corresponding temperature. As shown in Table 2, BET areas of the supported catalysts decrease with the addition of Mn (321 m^2/g) and specially after the addition of metal compared to that of HSAG (396 m^2/g). In addition, the pore volume is reduced by half for 2.5Cu2.5Ni-Mn/HSAG (0.23 cm^3/g) compared to that of HSAG (0.51 cm^3/g), presumably also due to the addition of MnO_2 and the reduced metal nanoparticles that form crystallites (Cu) that block the space formed by the aggregation of the graphite grains.

* Table 2 can be found in the Appendix section.

3.2 Surface Properties

3.2.1 TPD Measurements

The distributions of acidic sites were determined by TPD of NH_3 for selected samples (Fig. 6). All samples were reduced in situ with H_2 at 299.85ºC except 5Ni-Mn/HSAG, which was reduced at 450ºC. Therefore, the strength of acid sites was classified as weak (77 - 227ºC), medium (227 - 277ºC) and strong (277 - 402ºC), in accordance with other scales found with aluminium trioxide (Al_2O_3) and silicium dioxide (SiO_2) as supports, [63], [64].

* Figure 6 can be found in the Appendix section.

To obtain the distribution of acid strength, NH_3-TPD profiles of all samples were deconvoluted into three

components corresponding to weak, medium and strong acid sites. The acidity distribution derived after deconvolution of the NH_3-TPD profiles is presented in Table 3, taking into account the area of each TPD curve and the ones of the deconvoluted peaks. The normalized area of each curve in arbitrary units is also showed in Table 3 to compare the total acidity of the catalysts.

* Table 3 can be found in the Appendix section.

Table 3 shows a decrease in the amount of surface acid sites for the nanocomposites with respect Mn/HSAG sample. All samples show relatively uniform acid sites distribution while the acidity of 5Cu-Mn/HSAG and 2.5Cu2.5Ni-Mn/HSAG is predominantly associated to weak acid sites at 53% and at 41%, respectively (Fig. 6 and Table 3). Interestingly, the presence of Cu in 5Cu-Mn/HSAG noticeably increases the percentage of weak acid sites compared with the free-metal sample, while the addition of Ni in 2.5Cu2.5Ni-Mn/HSAG seems to decrease the amounts of weak sites associated to Cu and increase the amounts of strong sites associated to Ni since the sample 5Ni-Mn/HSAG show predominantly 36% strong acid sites. The bimetallic catalyst treated in He(g) at 450ºC shows an increase in the amount of medium strength acid sites compared to its counterpart without thermal treatment, while exhibiting quite uniform acid sites distribution, probably due to the incorporation of Cu and Ni into the structure of MnO_2 after this thermal treatment.

3.2.2 CO_2 Chemisorption Analysis Results

Strength and number of surface basic sites and their distribution were estimated for the catalysts by determination of CO_2 chemisorption heats. The evolution of the differential heat of adsorption with the surface coverage for the studied catalysts were shown in Fig. 7. The strength of basic sites can be classified as strong ($Q_{diff} > 90$ KJ/mol), medium ($90 > Q_{diff} > 60$ KJ/mol) and weak ($Q_{diff} < 60$ KJ/mol), whereas a differential heat of 40 kJ/mol is considered the limit between chemical and physical CO_2 adsorption, [65].

* Figure 7 can be found in the Appendix section.

Fig. 7a and 7b show similar distribution profiles of basic sites, although, there are some significant differences that must be taken into account. First of all, it is quite noticeable that the addition of Cu to the sample Mn/HSAG drops the total amount of basic sites to a half, while the percentage of strong basic sites remains practically the same (Table 4).

* Table 4 can be found in the Appendix section.

This latter finding is in agreement with the results of Leon et al., [66], that assessed the basicity of CuO, α-MnO_2 and Cu-Mn samples by CO_2-TPD and observed that the high temperature bands corresponding to strong basic sites of the single metal oxides shifted to slightly lower temperatures for the Cu-Mn samples accompanied with a decrease in the intensity of the signal, indicating that the total basicity was reduced for those catalysts. The addition of Ni has the opposite response: the total amount and the percentage of strong basic sites are higher than those of the Mn/HSAG sample. The combination of Cu and Ni (2.5Cu2.5Ni-Mn/HSAG) remarkably increases the total amount of basic sites (Table 3) compared to the samples with Cu and Ni alone, even though the percentage of strong basic sites is lower (42%) than the one achieved with 5Ni-Mn/HSAG (62%). Although, there are few studies approaching the effect of metal-MnO_2 interaction on the resulting material basicity, [67], [68], [69], [70], [71], regarding this effect on metal-MgO, suggest that the incorporation of metals in the MgO lattice has an improving effect in the basic surface of MgO. In addition to, the same interpretation could be applied to explain the effect of thermal treatment when metal is added on Mn containing catalysts.

3.2.3 TEM Analysis Results

TEM images of the catalysts and their corresponding histograms representing the particle size distribution are depicted in Fig. 8 and Fig. 9.

*Figure 8 can be found in the Appendix section.

TEM micrographs show Gaussian particle size distribution for all catalysts where the maximum of the peak coincides with the average particle size. Metallic particles supported over Mn/HSAG have bigger average particle sizes (d=11.1, 8.9 nm and 6.7 nm (Fig. 8a, 8b and 8c) than that of Cu/HSAG, Ni/HSAG and 2.5Cu2.5Ni/HSAG (d=11.7, 6.0, 7.8 and 11.5 nm (Fig. 9a, 9b and 9c), confirming the conclusions drawn from the X-ray study.

* Figure 9 can be found in the Appendix section.

3.2.4 EDX Analysis Results

EDX elemental mapping of the catalysts showed that Mn was highly dispersed on the support (Fig. 10a) and confirmed the formation of Cu and Ni NPs, which coincided in space with Mn evidencing well dispersion of the active phases over the carbonaceous support. The samples 5Cu-Mn/HSAG and 2.5Cu2.5Ni-Mn/HSAG reduced at 300ºC showed Cu particles of heterogeneous size (Fig. 10 and Fig. 11) in agreement with the size distribution determined by TEM (Fig. 9a and Fig. 9c),

while Ni and Mn remained well dispersed after reduction.

*Figure 10 can be found in the Appendix section.

3.2.5 XPS Analysis Results

In order to identify and quantify the different surface species of the catalysts, a surface analysis was carried out by XPS. All samples present essentially the same XPS spectra. For simplicity, Fig. 11 shows Mn $2p_{3/2}$, Cu $2p_{3/2}$ and Ni $2p_{3/2}$ core level spectra of catalyst 2.5Cu2.5Ni-Mn/HSAG after reduction in H_2 at 300ºC. The oxidation state observed for Mn $2p_{3/2}$ after its spectrum analysis is Mn^{+2}, having this species significant multiplet splitting according to literature, [72], [73].

*Figure 11 can be found in the Appendix section.

However, curve fitting of this species requires extremely good signal/noise of the spectra, the Mn $2p_{3/2}$ peak could only be deconvolved into three peaks corresponding with the peaks of maximum intensity representatives of Mn^{+2} and its characteristic shake-up. Binding energies of the three contributions observed for Mn $2p_{3/2}$ were practically constant for all the reduced samples (Table 5). A shoulder is evident on the Mn 2p spectra at ca 646 eV, evidencing the presence of Mn^{+2}, whose main peak appears at lower BE (641.1 eV), [72], [73], [74].

* Table 5 can be found in the Appendix section.

The catalysts studied showed two contributions for the Cu $2p_{3/2}$ peak corresponding to Cu^{+} (ca 932.9 eV) and Cu^{+2} (ca 934.5 eV) with its characteristic satellite at the high binding energy side, [75], [76], [77]. Cu^{+} was identified and differentiated from Cu^0 through observation of the L_3VV X-ray induced Auger parameter of Cu and the calculation of the modified Auger parameter, α'_A, which was defined as (Eq. 22):

$$\alpha'_A = h\nu + KE_{LMM} - KECu2p_{3/2} \quad (22)$$

where; KE_{LMM} and KE Cu $2p_{3/2}$ are the kinetic energies of the L_3VV X-ray induced Auger-emitted electrons and the Cu $2p_{3/2}$ photo-emitted electrons, respectively, [78]. The Auger parameters determined for all catalysts containing Cu (Table 5) are characteristic of Cu^{+} since α'_A is 1849.8 eV.

The formation of metallic Cu nanoparticles was confirmed by XRD and TEM analysis, the presence of Cu^{+2} is attributed to surface oxidation of the reduced sample under ambient air at room temperature (at 25ºC), while the core must remain Cu^0. Cu^{+} might be formed in the XPS chamber due to the reductive atmosphere which induces the reduction of surface Cu^{+2}. Ni $2p_{3/2}$ spectra of all samples exhibit a main peak at ca 855 eV corresponding to Ni^{+2} and a satellite peak at 861–862 eV. No peak could be ascribed to Ni^0 since its characteristic peak is associated to lower BE (852.6 eV). The Ni $2p_{3/2}$ envelope was fitted into two contributions at 853 - 854 eV and ca 855.9 eV, in agreement with other studies, [76], [79], [80]. Absence of Ni^0 could be attributed to surface oxidation to Ni^{+2}, as in the case of Cu.

XPS atomic ratios of Metal/C, Mn/C, Cu/Ni, and Metal/Mn for the samples studied are given in Table 5. The bimetallic sample reduced and after reaction shows higher Cu/Ni atomic ratio obtained by XPS, at 2.29 and at 1.48, respectively, than the nominal atomic ratio (Cu/Ni=0.92) (Table 6).

*Table 6 can be found in the Appendix section.

These results are consistent with literature, where surface Cu enrichment is observed for Cu-Ni nanostructured alloys, [81], and Cu-Ni supported over Al_2O_3, ZrO_2 and CeO_2/ZrO_2, [82], [83], due to the lower heat of sublimation of Cu compared to Ni that induce the former to occupy the surface sites of the particles.

3.3 1-Butanol Production from Ethanol

As is well known, a large volume of ethanol made from renewable carbon-neutral resources (i.e., biomass), called bioethanol, is being employed not only as a biofuel additive for gasoline, [84], [85], but also as a feedstock of various chemicals, [36], [86], [87], [88]. Approximately 98.4 billion liters of bioethanol was produced in 2018, [89]; however, its water solubility, corrosivity, and the differences in fuel properties between bioethanol and conventional transportation fuels (e.g., gasoline) make it unsuitable to employ ethanol fuel in modern internal combustion engines, [9].

Hence, the use of ethanol as the feedstock for the production of butanol has great potential. The process that converts ethanol to n-butanol is industrialized, which increases the carbon number by coupling two ethanol molecules. The Guerbet reaction is an aldol-condensation-type reaction of coupling alcohols, involving oxidation of alcohol to aldehyde, aldol condensation of the aldehyde to allyl aldehyde, and hydrogenation of the allyl aldehyde to its corresponding alcohol, [90]. For the reaction from ethanol to n-butanol, dehydrogenation of ethanol occurs first to make acetaldehyde, [91]. Aldol condensation of acetaldehyde to crotonaldehyde then takes place, followed by hydrogenation to form n-butanol, [92]. The conversion of ethanol to n-butanol is described in Fig. 12.

*Figure 12 can be found in the Appendix section.

Various homogeneous and heterogeneous catalysts are available for the Guerbet reaction. For the homogeneously-catalysed Guerbet reaction (taking place at 150–160^{o}C), ruthenium (Ru)-based or Mn-based homogeneous catalysts have been reported, [24], [31], [93], [94], [95], [96], [97]. Despite high ethanol selectivity (> 90%), the homogeneous Guerbet process leads to undesirable byproducts such Various homogeneous and heterogeneous catalysts are available for the Guerbet reaction. For the homogeneously-catalysed Guerbet reaction (taking place at 150–160°C), Ru-based or Mn-based homogeneous catalysts have been reported, [24], [31], [93], [94], [95], [96], [97]. Despite high ethanol selectivity (> 90%), the homogeneous Guerbet process leads to undesirable byproducts such as C_{6+} alcohols and sodium acetate, [32]. In addition, the separation of catalyst from the reaction product (i.e., butanol) is another issue of the homogeneous reaction, [98], [99], as C_{6+} alcohols and sodium acetate, [100]. In addition, the separation of catalyst from the reaction product (i.e., butanol) is another issue of the homogeneous reaction, [101], [102]. To avoid such problems, various heterogeneous catalyst systems that allow direct conversion of ethanol to n-butanol have been suggested, [5], [22], [89], [90], [101], [102].

Solid acid–base catalysts have been tested. For instance, a commercially available hydroxyapatite catalyst led to about 50% selectivity toward butanol at 350–440^{o}C with an indication of the formation. To avoid such problems, various heterogeneous catalyst systems that allow direct conversion of ethanol to n-butanol have been suggested, [5], [22], [90], [91], [92], [103]. Solid acid–base catalysts have been tested. For instance, a commercially available hydroxyapatite catalyst led to about 50% selectivity toward butanol at 350–440^{o}C with an indication of the formation of by-products such as H_2 and acetaldehyde, [104].

Kozlowski and Davis, [15], experimentally proved that an increase in the density of base sites on a ZrO_2 catalyst by an addition of 1 wt.% Na enhances the selectivity toward n-butanol because the dehydration of ethanol is significantly inhibited, [15], of by-products such as H_2 and acetaldehyde, [105]. Kozlowski and Davis experimentally proved that an increase in the density of base sites on a ZrO_2 catalyst by an addition of 1 wt.% Na enhances the selectivity toward n-butanol because, the dehydration of ethanol is significantly inhibited, [12].

Ogo et al., [18], synthesized four catalysts (Ca–P, Ca–V, Sr–P, and Sr–V) used for ethanol used for ethanol conversion to n-butanol. The ethanol conversion reaction was conducted at 300°C with a space velocity of 130 h.$g_{catalyst}$/$mol_{ethanol}$. The Strontium-Phosphorus (Sr-P) catalyst provided the highest selectivity toward n-butanol amongst the catalysts tested. This was because the Sr–P catalyst not only provided a high selectivity toward crotonaldehyde resulting from aldol condensation of acetaldehyde (an intermediate of n-butanol; Fig. 12) but also inhibited the coke formation occurring in the H_2 transfer reaction of 2-buten-1-ol into n-butanol. As the molar ratio of Sr/P became higher, the selectivity toward n-butanol was enhanced, [18]. The density of strong acid and base sites increased as the molar Sr/P ratio increased, and the base site density was much higher than the acid site density. Aldol condensation was expedited by base catalysis; thus, the Sr–P catalyst having a higher base site density resulted in a higher catalytic activity for the production of 1-butanol from ethanol, conversion to n-butanol, [13]. The ethanol conversion reaction was conducted at 300^{o}C with a space velocity of 130 h.$g_{catalyst}$/$mol_{ethanol}$. The Sr–P catalyst provided the highest selectivity toward n-butanol amongst the catalysts tested, [19].

3.3 Reaction Results

Blank experiments verified the absence of reaction at 230^{o}C either with the empty reactor or filled with silicon carbide, thus a catalyst is needed for the reaction to take place. The results obtained in the catalytic reaction for the different samples, once the steady state was reached, are shown in Table 7. Carbon balances for all samples were above 90%. Preliminary tests with the HSAG support and with Mn/HSAG sample show that these are inactive under the reaction conditions used.

*Table 7 can be found in the Appendix section.

As a general trend, the main products detected were 1-butanol, acetaldehyde, 1,1-diethoxy ethane, CO and CH_4, while other products observed in low quantities were ethyl acetate, 2-butanone, acetone, ethylene, ethane, pentane, propane, diethoxy butane, butanal, 2-butenal, 2-butanol, 2-ethyl-1-butanol, 1-hexanol, 1-octanol and 2-ethyl-1-hexanol. The presence of these compounds in the product stream is quite common for this condensation reaction, as can be seen by reviewing literature, although the relative amount of these compounds in the product distribution presents strong variations depending on the catalyst used. For example, 1,1-diethoxy ethane, ethyl acetate and other higher alcohols such as 1-hexanol and 1-octanol are the most common by-products, [15], [34], [53], [106], although acetone, ethylene, propane, pentane, butane and butene are also reported for this reaction, [12], [13], [36], [53], [65], [107], [108].

The catalysts were studied during 24 h of reaction and proved to be very stable in terms of conversion and 1-butanol selectivity. Fig. 13 shows that all catalysts reach a maximum in conversion at 3-4 h, followed by a

slight deactivation. Nevertheless, after 10 h the reaction achieves the steady state conditions.

*Figure 13 can be found in the Appendix section.

The XRD patterns of the bimetallic catalysts 4Cu1Ni-Mn/HSAG and 2.5Cu2.5Ni-Mn/HSAG reduced in H_2 at 300ºC and after reaction was shown in Fig. 14.

*Figure 14 can be found in the Appendix section.

For simplicity, samples after reaction are denoted with R - XRD patterns corresponding to the rest of catalysts samples reduced and after reaction at 230ºC and 49.40 atm can be found in the supplementary information (Fig. 15). The results show that the samples remained practically unchanged after reaction, though it can be observed that the peak corresponding to Cu^0 appears sharper for the samples after reaction, evidencing the sintering of Cu particles.

*Figure 15 can be found in the Appendix section.

In addition to, average particle size determined by TEM increases for all catalysts after reaction (Fig. 8 and Fig. 9), for the samples containing Cu, where the proportion of particles with a diameter bigger than 15 nm reaches 10% and 25% for 5Cu/HSAG and 5Cu-Mn/HSAG, respectively. The proportion of particles bigger than 15 nm after reaction is irrelevant for samples containing Ni alone and for 2.5Cu2.5Ni/HSAG. XRD and TEM results seem to conclude that the increase of particle size after reaction is due mainly to the sintering of Cu particles, for MnO_2 containing catalyst. Sun et al., [25], also observed an agglomeration of smaller nanoparticles to form bigger nanoparticles after reaction for catalysts containing Cu and Ni. It is interesting to note that 2.5Cu2.5Ni-Mn/HSAG treated in He(g) at 450ºC loses its Gaussian distribution after reaction and that more than 20% of the particles have a diameter superior than 15 nm. In Fig. 6b clearly showed an agglomeration of Ni and Mn for the sample 2.5Cu2.5Ni-Mn/HSAG after reaction at 230ºC, stable conversion after reaching a maximum at 3–4 h, all seems to indicate that Ni and specially Cu suffered superficial re-accommodation and agglomeration at early stages of the reaction prior to reaching the steady state conditions.

Atomic ratios extracted from the XPS analysis are in agreement with the conclusions drawn from the preceding characterization techniques (Table 5 and Fig. 9). The decrease of the Metal/C and Metal/Mn ratios clearly illustrates how Ni and especially Cu particles have bigger particle size after the chemical reaction at 230ºC and 49.4 atm. This effect is also observed for Mn comparing Mn/C ratios and the Mn mappings (Fig. 9a) where this element seems to agglomerate after reaction. These results confirm the conclusion derived from XRD, EDX and TEM analysis, given that some sintering of Cu NPs was observed after reaction for 5Cu/HSAG and 5Cu-Mn/HSAG samples, while less sintering or agglomeration of Ni particles was observed in the 5Ni-Mn/HSAG sample studied after reaction (Fig. 6b). XRD patterns of the support HSAG and the catalysts 4Cu1Ni-Mn/HSAG and 2.5Cu2.5Ni-Mn/HSAG was shown at Fig. 14, both reduced at 300ºC with H_2.

In order to understand the synergetic behaviour of the metals and Mn, it is of interest to analyse how both functions work separately. Despite showing negligible conversion, the main products with the sample Mn/HSAG were acetaldehyde, butane, 2-butenone, 1-butene, ethylene and ethane. These compounds were found in traces since more than 99% of the product stream was unreacted ethanol, the information deduced from these results is enough to conclude that Mn/HSAG sample is not capable of upgrading ethanol to 1-butanol, but it is promising as support since it contains acid/base sites of homogeneous strength distribution (Table 2 and Table 3) that are able to produce ethylene (formed by dehydration of ethanol on acid sites) and acetaldehyde (dehydrogenation of ethanol on base sites), among others.

Cu/HSAG, Ni/HSAG and 2.5Cu2.5Ni/HSAG show high activity for the conversion of ethanol but with low selectivity towards 1-butanol (4%, 7% and 4%, respectively), most likely due to the absence of base sites provided by Mn (Table 3). The principal by-products for Cu/HSAG were acetaldehyde and 1,1-dyethoxy ethane, which is formed by acid-catalysed acetylation of acetaldehyde with two ethanol molecules, [99]. Ni-HSAG tends to other undesired products such as CH_4, CO, diethyl ether, and acetone, whereas the bimetallic catalyst 2.5Cu2.5Ni/HSAG shows an intermediate behaviour between the monometallic Cu and Ni catalysts in terms of conversion and product distribution. Metal-catalysed acetaldehyde decarboxylation produces CH_4 and CO, [100]; diethyl ether is the product of the acid-catalysed ethanol dehydration, [36]; acetone is formed through ethyl acetate hydrolysis that produce acetic acid and subsequent centonizations of this compound, [57].

The three catalysts are very selective towards acetaldehyde, with a selectivity of 52% 5Cu/HSAG and 37% 2.5Cu2.5Ni/HSAG, respectively, which is consistent with literature since it is reported that Cu considerably speeds up the rate of ethanol dehydrogenation that leads to acetaldehyde, [57]. The presence of base sites would continue the reaction towards the aldol condensation of acetaldehyde that forms 3-hydroxybutanal, which readily dehydrates to 2-

butenal on acid sites and finally give rise to 1-butanol after subsequent hydrogenations, [14]. Since it was previously remarked that 1-butanol selectivity is insufficient with metal/HSAG, it seems that a good combination of metal with acid/base sites like those of Mn/HSAG (Table 3 and Table 4) would be a promising combination for the upgrading of ethanol towards 1-butanol.

Indeed, 1-butanol selectivity rise considerably when Cu and Ni are combined with Mn supported over HSAG presumably due to the combination of both functionalities: metal and acid/base sites. This enhancement is mainly observed with Cu since 1-butanol selectivity rises from 4% to 33% with 5Cu/HSAG and 5Cu-Mn/HSAG, respectively, while it increases from 7% to 21% with 5Ni/HSAG and 5Ni-Mn/HSAG, respectively. Despite containing more amounts of base sites (51 μmol CO_2 chemisorbed/g, 62% of high strength, Table 4) and more percentage of strong acid sites (38%, Table 3) than 5Cu-Mn/HSAG (22 μmol CO_2 chemisorbed/g, 45% of high strength, Table 4; 24% of strong acid sites, Table 3), 5Ni-Mn/HSAG is the worst catalyst in terms of 1-butanol selectivity (21%) among the bifunctional catalysts studied. It seems that the upgrading of ethanol to 1-butanol requires a good equilibrium of acid and base sites similar to that of 5Cu-Mn/HSAG, which is one of the samples studied that presented more acidity (Table 3), mainly of weak strength (53%, Table 3), and less basicity, mainly of high strength (62%, Table 4). It should be noted that ethanol conversion rises remarkably for both catalysts compared to their counterparts without Mn, and especially for 5Ni-Mn/HSAG which reaches 62% of ethanol conversion at pH=8.02, after 15 min. These clear differences in conversion may be attributed to the surface metal sites of the catalysts after reaction, since 5Ni-Mn/HSAG undergoes mild sintering (from 5.3 to 6 nm) compared to 5Cu-Mn/HSAG (from 8.3 to 11.7 nm). All things considered, acid/base sites are definitely necessary to catalyse the dehydration of 3-hydroxybutanal and the aldol condensation, respectively. But these centers do not seem to be as crucial as the number of exposed metal sites, which catalyses dehydrogenation/hydrogenation reactions, for achieving good conversion and consequently high 1-butanol yields.

Both catalysts present particularly different product distribution due to the before mentioned tendency of Ni to produce side reactions that lead to undesired by-products. 5Ni-Mn/HSAG constitutes an enhancement in the suppression of these side reactions since CO, CH_4 and acetone selectivity decrease from 11%, 24% and 12% with 5Ni/HSAG to 17%, 27% and 27% with 5Ni-Mn/HSAG, presumably because Mn covers the acid sites of the HSAG support and introduce basic sites. This sample presented less total amount of acid sites and a total amount of basic sites higher than Mn/HSAG and 5Cu-Mn/HSAG (Table 6 and Table 7). These by-products not found in the same catalyst with Cu instead of Ni, 5Ni-Mn/HSAG also produces low quantities of ethane, propane and pentane. 16% 5Cu-Mn/HSAG produces more 1,1-diethoxy ethane than 3% 5Ni-Mn/HSAG, respectively), but at the same time the presence of Mn reduces its formation compared to 33% 5Cu/HSAG. As the formation of 1,1-dyethoxy ethane requires acid sites, the different selectivity achieved for each catalyst are then consistent on the basis of their acidity, since the absence of Mn and the acid character of HSAG make 5Cu/HSAG more acid than 5Cu-Mn/HSAG, which in turn presents more acidity than 5Ni-Mn/HSAG (Table 6). Therefore, to inhibit the formation of undesired by-products and enhance the conversion and the selectivity towards 1-butanol, a catalyst combining the best characteristics attributed to Cu and Ni should improve the ethanol condensation route to 1-butanol.

The bimetallic catalysts studied present higher 1-butanol selectivity compared to the monometallic catalysts, especially 95% 2.5Cu2.5Ni-Mn/HSAG, which is 96% mostly of weak strength acid and 47% of strong basic sites compared to the other samples (Table 3 and Table 4). The catalytic behaviour of the 2.5Cu2.5Ni-Mn/HSAG is considerably better than that of its counterpart without Mn, 2.5Cu2.5Ni/HSAG, in terms of 1-butanol selectivity (that rises from 4% to 35%) and the formation of undesired byproducts, whose selectivity decrease when Mn is present in the catalyst formulation. This once again demonstrates that the presence of acid/base sites provided by MnO_2 is compulsory to satisfactorily upgrade ethanol towards 1-butanol. Ethanol conversion is higher 59% 2.5Cu2.5Ni-Mn/HSAG and 38% 4Cu1Ni-Mn/HSAG, respectively than the one achieved with 52% 5Cu-Mn/HSAG, but lower than that of 59% 5Ni-Mn/HSAG, which is consistent with the previous mentioned hypothesis that particle sintering during reaction severely affects ethanol conversion, since 6 nm of 5Ni-Mn/HSAG presents lower final particle size after reaction than 7.8 nm of 2.5Cu2.5Ni-Mn/HSAG, 8 nm of 4Cu1Ni-Mn/HSAG and 11.7 nm 5Cu-Mn/HSAG, respectively. However, considering both conversion and selectivity, it can be observed that the bimetallic catalysts improve the 1-butanol yield comparing to the monometallic and that the 2.5 wt.% Cu and 2.5 wt.% Ni is the optimal Cu-Ni load, thanks to the abovementioned compromise between medium-weak strength acid sites, homogeneous strength distribution of base sites and mild sintering. The presence of Ni enabled the 2.5Cu2.5Ni-Mn/HSAG catalyst to especially, reduce the formation of CO, CH_4, 1,1-diethoxy ethane and acetone, with selectivity of 9, 12, 5 and 15, respectively.

The 2.5Cu2.5Ni-Mn/HSAG catalyst treated in He(g) at 450°C slightly improved 1-butanol selectivity, but reduced considerably the ethanol conversion. This behaviour was expected due to the strong metal sintering observed after reaction (11.5 nm) and the reduction of its high strength acidity after thermal treatment, with 39% mostly weak and 32% medium strength acid sites, respectively (Table 7).

The favourable contribution of acid/base sites, the production of 1-butanol is strongly influenced by the metal function of the catalyst. In Fig. 16, the site time yield towards 1-butanol was calculated for the different Cu-Ni-Mn NCs samples based on the number of metal atoms on the surface/gram for the catalysts after reaction, since the superficial re-accommodation and agglomeration of Ni and Cu seems to be produced at early stages of the reaction prior to reaching the steady state conditions. The combination of Cu and Ni in the 2.5Cu2.5Ni-Mn/HSAG and especially in the 2.5Cu2.5Ni-Mn/HSAG* catalysts are the optimum among those studied to favour the reaction pathway towards 1-butanol (Fig. 16).

*Figure 16 can be found in the Appendix section.

3.4 Quantification

The yield (Y_i) of products was calculated based on the number of carbon atoms in the product as follows, where n_i represents the number of carbons and C_i is the molar concentration of the compound i, C_{EtOH} indicates concentration of ethanol before the reaction assuming the dilution with THF, (Eq. 23):

$$Y_i = \frac{n_i * C_i}{2 * C_{EtOH}} \quad (23)$$

Conversion was based on the number of carbon atoms in the compounds according to the equations below, where C_{EtOH} indicates concentration of ethanol before the reaction (assuming the dilution with THF) and C'_{EtOH} indicates concentration of ethanol after the reaction, (Eq. 24):

$$Conversion = 1 - \frac{C'_{EtOH}}{C_{EtOH}} \quad (24)$$

The selectivity of 1-butanol was defined as, (Eq. 25);

$$Selectivity\ (BuOH) = \frac{n_{BuOH} * C_{BuOH}}{\Sigma_i n_i C_i} \quad (25)$$

It should be pointed out that we identified most of the products in the liquid phase based on the gas chromatography-mass spectrophotometry (GC-MS) analysis. The carbon balance (C) was in the range 68%-99%, accounting for a loss of carbon materials in the gas phase and partly to the loss of liquid during transfer after reaction. The carbon balance was calculated as follows, (Eq. 26):

$$C = \frac{2C'_{EtOH} + \Sigma_i n_i C_i}{2C_{EtOH}} \quad (26)$$

Space time yield (STY) of 1-butanol was calculated as follows, where N_{EtOH} is the number of moles of ethanol before reaction, Y_{ButOH} is the yield of 1-Butanol, M_{ButOH} is the molar mass of 1-Butanol, $W_{cat.}$ is the weight of catalyst, and T is the reaction time, (Eq. 27):

$$STY = \frac{N_{EtOH} * Y_{ButOH} * M_{ButOH}}{2 * W_{Cat.} * T} \quad (27)$$

3.5 Leaching Test Results

The results of leaching tests during catalyst recycling for Cu-Ni-Mn NCs catalyst was determined at Table 8.

* Table 8 can be found in the Appendix section.

At the end of cycle 1, Cu concentration was measured as 0.6 mg/l, Ni concentration as 0.3 mg/l, and Mn concentration as 9.0 mg/l, respectively. The leaching process was completed at the end of cycle 9. At the end of cycle 9, Cu concentration was recorded as 0.2 mg/l, Ni concentration as 0.1 mg/l, and Mn concentration as 1.9 mg/l, respectively (Table 8).

3.6 Comparative Study of Catalytic Materials in the Ethanol to Butanol Reaction

The effect of reaction temperature on 1-butanol selectivity in a continuous-flow reactor was evaluated in the 170–300°C range for the 5Cu-Mn/HSAG catalyst. While ethanol conversion rises with increasing temperature, reaching 70% at 300°C, the highest 1-butanol selectivity (26%) is observed at 230°C. To further investigate the impact of temperature on product selectivity, it was presented the distribution of reaction products (1-butanol, acetaldehyde, 1,1-diethoxyethane, 2-butanone, 1-hexanol, and diethyl ether) for the 5Cu-Mn/HSAG catalyst. The selectivity trends observed in this study closely resemble those previously reported in the literature under similar temperature conditions using Cu-based and Ni-based catalysts, [23], [25], [60]. This selectivity pattern scan be explained by the formation of a primary product in a step wise reaction, which subsequently leads to undesired by-products at higher temperatures. The decline in acetaldehyde concentration above 230°C, can also be attributed to its further transformation in the reaction pathway. Additionally, selectivity to 1,1-diethoxyethane increases to 23%, consuming acetaldehyde, as this compound is produced via acid catalysed acetylation of acetaldehyde and ethanol, [101]. Other minor by-products with selectivity below 10% include 2-

butanone, 1-hexanol, and diethyl ether. Finally, the selectivity of unidentified products, which remains below 5% at temperatures under 230°C, shows a sharp increase to 24% at 300°C. In conclusion, the product distribution at temperatures below 230°C supports the proposed reaction mechanism was observed.

Since the highest 1-butanol selectivity was observed at 230°C, with high ethanol conversion and a carbon balance exceeding 90% in all cases, the catalyst screening was conducted at this temperature. Prior to these tests, blank reactions were carried out using HSAG as a support and Mn/HSAG, both of which exhibited negligible ethanol conversion at 230°C. Table 9 provides a summary of the catalytic performance of the various samples after 24 h, once the steady-state conditions were established.

* Table 9 can be found in the Appendix section.

As shown in Table 9, the composition of the catalysts plays a crucial role in determining the final product distribution. The identified products include 1-butanol, acetaldehyde, 1,1-diethoxyethane, CO, CH_4, and several minor by-products, such as 2-butenal, 2-butanone, ethyl acetate, ethylene, 1-hexanol, butanal, diethoxy butane, 1-octanol, 2-butanol, 2-ethyl-1-butanol, 2-ethyl-1-hexanol, and acetone. While CH_4 and CO are formed through acetaldehyde decarbonylation, a reaction facilitated by metallic catalysts, acetone is generated via ketonization of acetic acid, which itself results from the hydrolysis of ethyl acetate, [57], [102], [109]. Notably, after 24 h of reaction, the catalysts demonstrated high stability in terms of 1-butanol selectivity. This figure also highlights that conversion and butanol selectivity undergo changes during the initial 5–6 h of reaction. After this period, a slight deactivation is observed, though the butanol selectivity values remain stable. The initial fluctuations in conversion and selectivity suggest that the catalyst surfaces undergo modifications during the early stages of reaction at 230°C and 48.36 atm. Moreover, a comparison of average particle sizes between fresh and spent catalysts, summarized in Table 8, confirms that some degree of nanoparticle sintering occurs throughout the reaction.

3.7 Plug Flow Reactor (PFR) Results

The material balance in the plug flow reactor (PFR) is as follows:

* Figure 17 can be found in the Appendix section.

For a molar flow rate of 1000 mol/h, the material balance is show in Eq. (28), Eq. (29), Eq. (30), and Eq. (31):

$$ACC = IN - OUT + GEN - CONS \quad (28)$$

$$CH_3OH: 0 = 100 - n_{CH_3OH}^{out} + \varepsilon - 2\varepsilon \leftrightarrow n_{CH_3OH}^{out} = 1000 - 2\varepsilon \quad (29)$$

$$H_2O: 0 - n_{H_2O}^{out} + \varepsilon - 0 \leftrightarrow n_{H_2O}^{out} = \varepsilon \quad (30)$$

$$CH_3OCH_3: 0 = 0 - n_{CH_3OCH_3}^{out} + \varepsilon - 0 \leftrightarrow n_{CH_3OCH_3}^{out} = \varepsilon \quad (31)$$

For a conversion of 0.66:

$$0.66 = \frac{1000 - 1000 + 2\varepsilon}{1000} \rightarrow 660 = 2\varepsilon$$

$$\varepsilon = 330\ mol/h$$

From where $\begin{cases} n_{H_2O}^{out} = n_{CH_3OCH_3}^{out} = 330\frac{mol}{h} \\ n_{CH_3OH}^{out} = 340\ mol/h \end{cases}$

3.7.1 Equilibrium Constant

The equilibrium constant is given as follows:

$$[H_2O] = \frac{\varepsilon}{1000}P_t$$

$$[CH_3OCH_3] = \frac{\varepsilon}{1000}P_t$$

$$[CH_3OH] = \frac{100-2\varepsilon}{1000}P_t$$

$$K_{eq} = \frac{\varepsilon^2}{(1000-2\varepsilon)^2}$$

$$K_{eq} = 0.94$$

3.8 Determination of the Temperature in the Reactor

In chemistry, equilibrium constant characterizes the state of equilibrium of a chemical system, with the value of the latter dependent on the reaction considered and the temperature in order to predict the direction of evolution of the system (Table 10).

* Table 10 can be found in the Appendix section.

It is noted that the progression of the reaction is effective at the temperature range going from 300°K to 650°K (data not shown). Once exceeded, there is a regression of the reaction as indicated by the bending on the curve, which this time stabilizes and remains constant from 700°K up to above 1000°K.

The volume of the reactor is obtained by the following relation in Eq. (5), Eq. (6) and Eq. (7):

$$V_R = F_{A0}\int_0^{X_{AF}} \frac{dX_A}{-r_A} \quad (5)$$

$$C_A = \frac{P}{RT} \quad (6)$$

$$-r_A = kC_A^2 \quad (7)$$

Where F_{A0}=0.28 moles; P=1346.868 Pa; R=8.314 m^3.Pa/mol.^oK; k=1.00; C_A=0.27 mol/m^3; T=600^oK; -r_A=0.077 mol/m^3.s; X_{AF}=0.67; and V_R=2.43 m^3.

Hence to calculate the residence time in the reactor, the following relation was used in Eq. (32) and Eq. (33)

$$\tau = \frac{V_R}{V_o} \quad (32)$$

$$V_0 = \frac{m}{p} \quad (33)$$

Having = 11.24 m^3/s and the volume of the reactor, the residence time is = 0.22 s.

3.9 Calculation of the Mass of the Catalyst and the Volume of the PBR

The mechanism involved in the methanol to gasoil process is quite complex. A simplified reaction scheme (proposed by Chang and Silvestri, [109]) is shown as follows in Eq. (34):

$$2CH_3OH \leftrightarrow \underset{+H_2O}{\overset{-H_2O}{CH_3OCH_3}} \rightarrow \overset{-H_2O}{C_2 - C_5 alkanes} \rightarrow alkanes, cycloalkanes\ and\ aromatics \quad (34)$$

The product selectivity measured as a function of a wide range of contact time (data not shown). The latter measures the contact time between the catalyst and the reagent molecules. At the smallest contact time, that is, in the order of 10^{-3} hours, water and dimethyl ether are the main products obtained. When the contact time increases, the production of dimethyl ether finally reaches a maximum and then decreases. From the methyl ether, there is now a high probability of further dehydration to give the alken products. With further increase in contact time, alkanes / + alkenes and aromatics are obtained, [41], (Fig.18).

* Figure 18 can be found in the Appendix section.

Indeed knowing the residence time and the space speed by analogy, the volume of the reactor is deduced by the following relation in Eq. (11) and Eq. (12):

$$V_{PBR} = \tau\, x\, V_0 \quad (11)$$

$$V_0 = F_A\, x\, V_m \quad (12)$$

Having considered – r_{oxy}=0.00176 mol/kg_{cat}.s; WHSV=0.000278 s^{-1}; F_{oxy}=0.186 mol/s; x_A=0.43; M_{mA}=0.068 kg/mol, we obtained W_{cat}=45.52 kg; F_A=1000 mol/h; τ=1 h; V_{PBR}=24.4 m^3.

At Eq. (8):

$$W_{cat} = \frac{F_{A0} \int_0^x x_A}{-r_{oxy}} \quad (8)$$

Where, *W*, is the mass of the catalyst required to reduce the molar feed rate of *A*, F_{A0} for a conversion x_A, Eq. (9), [40] and Eq. (10), [41]:

$$V_{cat} = \frac{W_{cat}}{\rho_{cat}} \quad (9)$$

$$-r_{oxy} = x_A \frac{WHSV}{Mm_A} \cdot \left(\frac{1h}{3600s}\right) \quad (10)$$

According to the graph in Figure 5, the hydrocarbons are obtained in a residence time of about one hour in the reactor from the experiments of Chang and Silvestri, [109]. Fig. 19 gives the volume of the PFR reactor as a function of the fractional conversion of methanol. The volume of the reactor is proportional to the fractional conversion whereas its growth is linear for the PFR. With a fractional conversion=0.90, the volume of the PFR reactor=3.28 m^3. However, for the feed equilibrium mixture, the desired fractional conversion = 0.67 and the reactor volume=2.43 m^3, for a pressure of 1346.868 Pa and a temperature of 600^{o}K.

* Figure 19 can be found in the Appendix section.

Fig. 20 gives the effect of the concentration of methanol on the volume of the PFR. The change in the volume of the reactor is linear; the greater the concentration of methanol, the greater is the volume of said reactor; it has an optimum concentration=0.27 mole/m^3 for which P = 1346.868 Pa and T=600^{o}K; and the volume of the reactor is 2.43 m^3.

* Figure 20 can be found in the Appendix section.

Fig. 21gives the mass of the catalyst as a function of the conversion of dimethyl ether and methanol to hydrocarbons. The mass remains constant with the variation of the oxygenate conversion rate. For example, for a conversion of 0.43, the mass of the catalyst remains 45.52 kg.h is also the case for a constant reactor volume of 24.4 m^3 and for a reaction rate of 0.00327 mol/kgcat.s.

* Figure 21 can be found in the Appendix section.

As regards PBR where the reactions are complex with several kinds of mechanisms established by different authors, however, the model established by

Rojas, [110], made the task simpler in terms of the reaction kinetics related to our second reactor.

The physicochemical analysis of the inputs of the PFR and the PBR provided several elements sufficiently necessary in the meticulous approach of the dimensioning, starting in fact, by the establishment of the material balance around the PFR. However, the fractional conversion of methanol into DME can reach 0.9, the feed into the PBR required equilibrium mixing of methanol/ DME/water since for an infinitely small residence time the conversion of unconverted methanol into PFR continued in the PBR until an almost complete conversion is reached (Fig. 22).

* Figure 22 can be found in the Appendix section.

Thus, for this process, therefore knowing the course in the reactors, the fractional conversion established was therefore 0.67 (which can also reach 0.75 for other authors) in the PFR reactor, [111].

Here the gas produced by the gasifier is a renewable fuel and the power produced by its combustion is renewable. When the fuel to the gasifier is a waste stream, its conversion to power in this manner has the combined benefit of the conversion of this waste into useful products as biofuel route of methanol to gasoline process. The wealth of the DRC in natural resources offers a striking contrast with the poverty of its population.

4 Conclusions

Cu-Ni-and MnO_2 NCs supported over HSAG were screened in a fixed-bed gas continuous reactor to study the conversion of ethanol to 1-butanol. Their catalytic performance showed substantial differences that were tentatively explained by characterization of the active sites by TPD of NH_3, microcalorimetry of CO_2 chemisorption and TEM/EDX analysis, which provided information about the acid/base sites related to MnO_2 and its interaction with the metal particles, and the dehydrogenating/hydrogenating properties associated (plug flow reactor and packed bed reactor) for the production of 1-butanol from ethylene alcohol. He revealed the importance of the process and various advantages of the latter, mainly from a technical point of view; in fact, the development of a process requires several prerequisites for highlighting the process from design to synthesis (Complete process). This approach helped to orient in a more objective sense what has been the aim of this work. Determination of the volume of the PBR revealed that the latter depends on the molar feed rate when the molar volume is considered at the standard condition of temperature and pressure (CSTP.) The biggest problem was determining the reaction rate for the methanol / DME mixture conversion to hydrocarbons, in order to deduce the mass of the catalyst. The latter has been shown, to be independent of methanol / DME conversion. The yield of the process was 43% of the methanol / DME mixture mass entering the PBR. Different topological optimization experiments could improve this efficiency since it is proportional to the conversion of the methanol / DME mixture.to Cu-Ni particle size and distribution. These analysis and catalytic tests suggested the existence of a synergetic effect between Mn combined with Cu and/or Ni dispersed over HSAG that gives place to an improved catalyst, in terms of high 1-butanol yield, when applied in the Guerbet process. Cu is needed since it considerably speeds up the rate of ethanol dehydrogenation that leads to acetaldehyde, while nickel's activity and less disposition to sintering favoured the ethanol conversion, although more undesired products and mostly gases were produced.

Bimetallic catalysts proved to combine the best characteristics of both metals. The most promising catalyst, 2.5Cu2.5Ni-Mn/HSAG* treated in He(g) at 450^{o}C prior reduction with H_2, exhibited 62% ethanol conversion and the maximum 1-butanol production yield was 96% at an ethanol concentration of 4 mg/l at 2 mg/l Cu-Ni-Mn-NCs concentration at a Mn percentage of 18% after 15 min at a pH of 8.02. High amounts of weak acid sites and strong basic sites was constituted the optimal acid/base site strength distribution. Its higher metal particle size after reaction seems to provide a slightly negative impact in ethanol conversion. The catalyst has proven robust without significant deactivation over 7 cycles. Structural characterization before and after reaction revealed the formation of metal nanoparticles as well as the existence of a Ni-Cu-Mn alloy phase that likely plays a role in the excellent catalytic performance.

Even though, the employment of a range of heterogeneous catalysts for the conversion of ethanol to n-butanol has been extensively investigated, evaluation of all available catalytic systems that upgrade ethanol to butanol in terms of economic and environmental points of view is necessary because the technologies are able to aid in high-quality fuel production in an environmentally-friendly way. The evaluation, however, is not easily achieved on a lab scale. Therefore, the studies to evaluate catalyst performance at an industrial scale need to be carefully conducted.

Moreover, this catalyst remarkably reduces the formation of unwanted products. For all catalysts, the analysis of the product streams indicated that the reaction pathway follows the Guerbet reaction demonstrated good stability, remaining active for 24 h on stream. Acid/base sites have a considerably impact on 1-butanol selectivity and product distribution, it seems that the metal function plays a crucial role in the Guerbet ethanol condensation reaction since clear

differences in conversion are attributed to the sintering of particles that leads to decreasing conversion. Therefore, a compromise between both parameters must be reached to further optimize these catalysts. Cu-Ni-Mn-NCs was affected for 1-butanol production from the ethanol producing industry wastes.

Acknowledgement:
Experimental analyzes in this study were performed at the Laboratories of the Canada Research Center, Ottawa, Canada. The authors would like to thank this body for providing financial support.

References:

[1] A. Demirbas, Biofuels Securing the Planet's Future Energy Needs, *Energy Conversion and Management*, Vol.50, No.9, 2009, pp. 2239-2249.

[2] T. W. Patzek, Thermodynamics of the Corn-Ethanol Biofuel Cycle, *Critical Reviews in Plant Sciences*, Vol.23, No.6, 2004, pp. 519-567.

[3] A. T. Nielsen, W. J. Houlihan, The Aldol Condensation, *Organic Reactions*, Vol.1, 1968, pp. 1-438.

[4] G. Onyestyák. Carbon Supported Alkaline Catalysts for Guerbet Coupling of Bioethanol, *Periodica Polytechnica Chemical Engineering*, Vol.62, No.1, 2018, pp. 91–96.

[5] J. H. Earley, R. A. Bourne, M. J. Watson, M. Poliakoff. Continuous Catalytic Upgrading of Ethanol to n-Butanol and $>C_4$ Products over Cu/CeO_2 Catalysts in Supercritical CO_2, *Green Chemistry*, Vol.17, No.5, 2015, pp. 3018–3025.

[6] X.Zhang, Z. Liu, X. Xu, H. Yue, G. Tian, S. Feng, Hydrothermal Synthesis of 1-Butanol from Ethanol Catalyzed with Commercial Cobalt Powder, *ACS Sustainable Chemistry & Engineering*, Vol.1, 2013, pp. 1493-1497.

[7] B. Ndaba, I. Chiyanzu, S. Marx, n-Butanol Derived from Biochemical and Chemical Routes: A Review, *Biotechnology Reports (Amsterdam),* Vol.8, 2015, pp. 1-9.

[8] T. Tsuchida, S. Sakuma, T. Takeguchi, W. Ueda, Direct Synthesis of n-Butanol from Ethanol over Nonstoichiometric Hydroxyapatite, *Industrial & Engineering Chemistry Research*, Vol.45, 2006, pp. 8634-8642.

[9] A. Galadima, O. Muraza, Catalytic Upgrading of Bioethanol to Fuel Grade Biobutanol: A Review, *Industrial & Engineering Chemistry Research*, Vol.54, 2015, pp. 7181-7194.

[10] W. Ueda, T. Kuwabara, T. Ohshida, Y. Morikawa, A low-pressure guerbet reaction over magnesium oxide catalyst, *Journal of the Chemical Society, Chemical Communications*, 1990, pp. 1558-1559.

[11] A. S. Ndou, N. Plint, N. J. Coville, Dimerisation of Ethanol to Butanol over Solid-Base Catalysts, *Applied Catalysis A: General*, Vol.251, 2003, pp. 337-345.

[12] J. Kozlowski, R. Davis, Heterogeneous Catalysts for the Guerbet Coupling of Alcohols, *ACS Catalysis,* Vol.3, 2013a, pp. 1588-1600.

[13] J. Kozlowski, R. Davis, Sodium Modification of Zirconia Catalysts for Ethanol Coupling to 1-Butanol, *International Journal of Energetic Materials and Chemical Propulsion*, Vol.22, 2013b, pp. 58-64.

[14] I. C. Marcu, N. Tanchoux, F. Fajula, D. Tichit, Catalytic Conversion of Ethanol into Butanol over M–Mg–Al Mixed Oxide Catalysts (M = Pd, Ag, Mn, Fe, Cu, Sm, Yb) Obtained from LDH Precursors, *Catalysis Letters*, Vol.143, 2013, pp. 23-30.

[15] J. Scalbert, F. Thibault-Starzyk, R. Jacquo, D. Morvan, F. Meunier, Ethanol Condensation to Butanol at High Temperatures over a Basic Heterogeneous Catalyst: How Relevant is Acetaldehyde Self-Aldolization?, *Journal of Catalysis*, Vol.311, 2014, pp. 28-32.

[16] K. Koda, T. Matsu-ura, Y. Obora, Y. Ishii, Guerbet Reaction of Ethanol to n-Butanol Catalyzed by Iridium Complexes, *Chemistry Letters*, Vol.38, No.8, 2009, pp. 838-839.

[17] S. Ordóñez, E. Díaz, M. León, L. Faba, Hydrotalcite-Derived Mixed Oxides as Catalysts for Different C–C Bond Formation Reactions from Bioorganic Materials, *Catalysis Today*, Vol.167, No.1, 2011, pp. 71-76.

[18] S. Ogo, A. Onda, K. Yanagisawa, Selective Synthesis of 1-Butanol from Ethanol over Strontium Phosphate Hydroxyapatite Catalysts, *Applied Catalysis A: General*, Vol.402, No.1-2, 2011, pp. 188-195.

[19] S. Ogo, A. Onda, Y. Iwasa, K. Hara, A. Fukuoka, K. Yanagisawa, 1-Butanol Synthesis from Ethanol over Strontium Phosphate Hydroxyapatite Catalysts with Various Sr/P Ratios, *Journal of Catalysis*, Vol.296, 2012, pp. 24-30.

[20] T. Riittonen, E. Toukoniitty, D. K. Madnani, A. R. Leino, K. Kordas, M. Zabo, A. Sapi, K. Eränen, P. Mäki-Arvela, A. Shchukarev, A.-R. Rautio, K. Kordas, N. Kumar, T. Salmi, J.-P. Mikkola, Continuous Liquid-Phase Valorization of Bio-Ethanol towards Biobutanol over Metal Modified Alumina, *Renewable Energy*, Vol.74, 2015, pp. 369-378.

[21] P. Dziugan, K. G. Jastrzabek, M. Binczarski, S. Karski, A. Witonska, B. Kolesinska, Z. J. Kaminski, Continuous Catalytic Coupling of Raw

Bioethanol into Butanol and Higher Homologues, *Fuel*, Vol.158, 2015, pp. 81-90.

[22] J. Pang, M. Zheng, L. He, L. Li, X. Pan, A. Wang, X. Wang, T. Zhang, Upgrading ethanol to n-butanol over highly dispersed Ni-MgAlO catalysts, *Journal of Catalysis*, Vol.344, 2016, pp. 184-193.

[23] J. Quesada, L. Faba, E. Díaz, S. Ordóñez, Tuning the Selectivities of Mg-Al Mixed Oxides for Ethanol Upgrading Reactions through the Presence of Transition Metals, *Applied Catalysis A: General*, Vol.559, 2018, pp. 167-174.

[24] S. Chakraborty, P. E. Piszel, C. E. Hayes, R. T. Baker, W. D. Jones, Highly Selective Formation of n-Butanol from Ethanol through the Guerbet Process: A Tandem Catalytic Approach, *Journal of the American Chemical Society*, Vol.137, 2015, pp. 14264-14267.

[25] Z. Sun, A. C. Vasconcelos, G. Bottari, M. C. A. Stuart, G. Bonura, C. Cannilla, F. Frusteri, K. Barta, Efficient Catalytic Conversion of Ethanol to 1-Butanol via the Guerbet Reaction over Copper- and Nickel-Doped Porous, *ACS Sustainable Chemistry & Engineering*, Vol.5, No.2, 2017, pp. 1738-1746.

[26] E. Díaz, S. Ordónez, F. Bueres, E. Asedegbega-Nieto, H. Sastre, High-Surface Area Graphites as Supports for Hydrodechlorination Catalysts: Tuning Support Surface Chemistry for an Optimal Performance, *Applied Catalysis B: Environment and Energy*, Vol.99, No.1-2, 2010, pp. 181-190.

[27] J. L. Eslava, X. Sun, J. Gascon, F. Kapteijn, I. Rodríguez-Ramos, Ruthenium Particle Size and Cesium Promotion Effects in Fischer–Tropsch Synthesis over High-Surface-Area Graphite Supported Catalysts, *Catalysis Science & Technology*, Vol.7, 2017, pp. 1235-1244.

[28] L. Faba, E. Díaz, S. Ordoñez, Gas Phase Acetone Self-Condensation over Unsupported and Supported Mg–Zr Mixed-Oxides Catalysts, *Applied Catalysis B: Environment and Energy*, Vol.142–143, 2013a, pp. 387-395.

[29] L. Faba, E. Díaz, S. Ordoñez, Improvement on the Catalytic Performance of Mg–Zr Mixed Oxides for Furfural–Acetone Aldol Condensation by Supporting on Mesoporous Carbons, *ChemSusChem*, Vol.6, 2013b, pp. 463-473.

[30] H. S. Ghaziaskar, C. Xu, One-Step Continuous Process for the Production of 1-Butanol and 1-Hexanol by Catalytic Conversion of Bio-Ethanol at Its Sub-/Supercritical State, *RSC Advances*, Vol.3, 2013, pp. 4271-4280.

[31] S. Fu, Z. Shao, Y. Wang, Q. Liu, Manganese-Catalyzed Upgrading of Ethanol into 1-Butanol, *Journal of the American Chemical Society*, Vol.139, No.34, 2017, pp. 11941-11948.

[32] N. V. Kulkarni, W. W. Brennessel, W. D. Jones, Catalytic Upgrading of Ethanol to n-Butanol via Manganese-Mediated Guerbet Reaction, *ACS Catalysis*, Vol.8, No.2, 2018, pp. 997-1002.

[33] V. Nagarajan, N. R. Kuloor, Catalytic Preparation of n-Butanol from Ethanol in One Step, Indian *Journal of Technology*, Vol.4, 1966, pp. 46-54.

[34] F. Engelhardt, W. Schritt, *Method of Producing β Branched Aldehydes*, US Patent 3558716 A;1971, 1971.

[35] Y. Kitayama, A. Michishita, Catalytic Activity of Fibrous Clay Mineral Sepiolite for Butadiene Formation from Ethanol, *RSC Journal of the Chemical Society, Chemical Communications*, Vol.9, 1981, pp. 401-402.

[36] E. Makshina, M. Dusselier, W. Janssens, J. Degrève, P. Jacobs, B. Sels, Review of Old Chemistry and New Catalytic Advances in the On-Purpose Synthesis of Butadiene, *RSC Chemical Society Reviews*, Vol.43, No.22, 2014, pp. 7917-7953.

[37] T. D. Matson, K. Barta, A. V. Iretskii, P. C. Ford, One-Pot Catalytic Conversion of Cellulose and of Woody Biomass Solids to Liquid Fuels. *Journal of the American Chemical Society*, Vol.133, No.35, 2011, pp. 14090-14097.

[38] K. Barta, Efficient Catalytic Conversion of Ethanol to 1-Butanol via the Guerbet Reaction over Copper- and Nickel-Doped Porous, *ACS Sustainable Chemistry & Engineering*, Vol.5, No.2, 2017, pp. 1738-1746.

[39] J. R. Couper, *Chemical Process Equipment Selection and Design*, Third Edition, 2012.

[40] P. Diagbonia, O. E. Ehirim, Design Flow Reactors for Production of Dimethyl Ether, *American Journal of Engineering Research*, Vol.8, No.8, 2019, pp. 70-83.

[41] A. Rosen, *Reactor Design*, TUFTS Chemical Engineering Review Guide Available at: http://sites. tufts. edu/andrewrosen/files/2013/09/reactor_design_guide1. pdf, 2014.

[42] E. Gallegos-Suarez, A. Guerrero-Ruiz, I. Rodriguez-Ramos, A. Arcoya, Comparative Study of the Hydrogenolysis of Glycerol over Ru-Based Catalysts Supported on Activated Carbon, Graphite, Carbon Nanotubes and KL-Zeolite, *Chemical Engineering Journal*, Vol.262, 2015, pp. 326-333.

[43] B. Bachiller-Baeza, I. Rodriguez-Ramos, A. Guerrero-Ruiz, Interaction of Carbon Dioxide with the Surface of Zirconia Polymorphs, *Langmuir*, Vol.14, No.13, 1998, pp. 3556-3564.

[44] J. R. Anderson, Particle Size Effects in Metal Catalysts, *Science Progress*, Vol.69, No.276, 1985, pp. 461-484.

[45] B. Lu, S. Ma, S. Liang, Z. Wang, Y. Liu, S. Mao, H. Ban, L. Wang, Y. Wang, Efficient Conversion of Ethanol to 1-Butanol over Adjacent Acid–Base Dual Sites via Enhanced C–H Activation, *ACS Catalysis*, Vol.13, 2023, pp. 4866–4872.

[46] J. Sun, Y. Wang, Recent Advances in Catalytic Conversion of Ethanol to Chemicals, *ACS Catalysis*, Vol.4, 2014, pp. 1078–1090.

[47] W. C. Wang, L. Tao, Bio-Aviation Fuel Conversion Technologies, *Renewable and Sustainable Energy Reviews*, Vol.53, 2016, pp. 801–822.

[48] M. León, E. Díaz, S. Ordóñez, Ethanol Catalytic Condensation over Mg-Al Mixed Oxides Derived from Hydrotalcites, *Catalysis Today*, Vol.164, 2011, pp. 436–442.

[49] I. C. Marcu, D. Tichit, F. Fajula, N. Tanchoux, Catalytic Valorization of Bioethanol over Cu-Mg-Al Mixed Oxide Catalysts, *Catalysis Today*, Vol.147, 2009, pp. 231–238.

[50] C. R. Ho, S. Shylesh, A. T. Bell, Mechanism and Kinetics of Ethanol Coupling to Butanol over Hydroxyapatite, *ACS Catalysis*, Vol.6, 2016, pp. 939–948.

[51] K. Shimizu, Heterogeneous Catalysis for the Direct Synthesis of Chemicals by Borrowing Hydrogen Methodology, *Catalysis Science & Technology*, Vol.5, 2015, pp. 1412–1427.

[52] J. H. Zar, Biostatistical Analysis, Prentice-Hall, Englewood Cliffs, 1984.

[53] Statgraphics Centurion XV, Sofware, StatPoint Inc, Statgraphics Centurion XV, Herndon, VA, USA, 2005.

[54] V. Thyssen, T. Maia, E. Assaf, Cu and Ni Catalysts Supported on γ-Al_2O_3 and SiO_2 Assessed in Glycerol Steam Reforming Reaction, *Journal of the Brazilian Chemical Society*, Vol.26, No.1, 2015, pp. 22-31.

[55] A. B. Dongil, B. Bachiller-Baeza, I. Rodríguez-Ramos, J. L. G. Fierro, N. Escalona, The Effect of Cu Loading on Ni/Carbon Nanotubes Catalysts for Hydrodeoxygenation of Guaiacol, *RSC Advances*, Vol.6, 2016, pp. 26658-26667.

[56] D. Lopes, F. Zotin, L. A. Palacio, Copper-Nickel Catalysts from Hydrotalcite Precursors: The Performance in NO Reduction by CO, *Applied Catalysis B: Environment and Energy*, Vol.237, 2018, pp. 327-338.

[57] A. Guerrero-Ruiz, A. Sepúlveda-Escribano, I. Rodríguez-Ramos, Carbon Monoxide Hydrogenation over Carbon Supported Cobalt or Ruthenium Catalysts. Promoting Effects of Magnesium, Vanadium and Cerium Oxides, *Applied Catalysis A: General*, Vol.120, No.1, 1994, pp. 71-83.

[58] L. Gonzalo-Chacón, M. Almohalla, E. Gallegos-Suarez, A. Guerrero-Ruiz, I. Rodríguez-Ramos, L. Ryan, F. Convery, S. Ferreira, Stimulating the Use of Biofuels in the European Union: Implications for Climate Change Policy, *Energy Policy*, Vol.34, No.17, 2006, pp. 3184-3194.

[59] G. Peng, F. Gramm, C. Ludwig, F. Vogel, Effect of Carbon Surface Functional Groups on the Synthesis of Ru/C Catalysts for Supercritical Water Gasification, *Catalysis Science & Technology*, Vol.5, 2015, pp. 3658-3666.

[60] M. Cerro-Alarcón, B. Bachiller-Baeza, A. Guerrero-Ruiz, I. Rodríguez-Ramos, Effect of the Reduction–Preparation Method on the Surface States and Catalytic Properties of Supported-Nickel Particles, *Molecular Catalysis*, Vol.258, No.1-2, 2006, pp. 221-230.

[61] M. Cerro-Alarcon, A. Guerrero-Ruiz, I. Rodriguez-Ramos, Stereoselective Hydrogenation of Paracetamol to Trans-4-Acetamidocyclohexanol on Carbon-Supported Ru-M (M = Co, Ni) Bimetallic Catalysts, *Catalysis Today*, Vol.93–95, 2004, pp. 395-403.

[62] T. Jordison, C. Lira, D. Miller, Condensed-Phase Ethanol Conversion to Higher Alcohols, *Industrial & Engineering Chemistry Research*, Vol.54, 2015, pp. 10991-11000.

[63] P. T. Patil, D. Liu, Y. Liu, J. Chang, A. Borgna, Improving 1, 3-Butadiene Yield by Cs Promotion in Ethanol Conversion, *Applied Catalysis A: General*, Vol.543, 2017, pp. 67-74.

[64] M. León, E. Díaz, S. Bennici, A. Vega, S. Ordónez, A. Auroux, Adsorption of CO_2 on Hydrotalcite-Derived Mixed Oxides: Sorption Mechanisms and Consequences for Adsorption Irreversibility, *Industrial & Engineering Chemistry Research*, Vol.49, No.8, 2010, pp. 3663-3671.

[65] M. León, E. Díaz, A. Vega, S. Ordóñez, A. Auroux, Consequences of the Iron–Aluminium Exchange on the Performance of Hydrotalcite-Derived Mixed Oxides for Ethanol Condensation, *Applied Catalysis B: Environment and Energy*, Vol.102, 2011, pp. 590-599.

[66] W. Ueda, H. Kurokawa, Y. Morooka, T. Ikawa, Coupling Reaction between Methyl Propionate and Methanol to Form Methyl Methacrylate over Metal Ion-Containing Magnesium Oxide Catalysts, *Chemistry Letters*, Vol.6, 1985a, pp. 819-820.

[67] W. Ueda, T. Yokoyama, Y. Moro-oka, T. Ikawa, Catalytic Synthesis of Vinyl Ketones over Metal Oxide Catalysts Using Methanol as the Vinylating Agent, *Chemistry Letters*, Vol.1, 1984, pp. 39-40.

[68] W. Ueda, T. Yokoyama, Y. Morooka, T. Ikawa, Enhancement of Surface Base Property of

Magnesium Oxide by the Combination of Metal Ion, *Chemistry Letters*, Vol.14C, 1985b, pp. 1059-1062.

[69] R. Ferrando, A. Fortunelli, Diffusion of Adatoms and Small Clusters on Magnesium Oxide Surfaces, *Journal of Physics: Condensed Matter*, Vol.21, No.26, 2009, 264001.

[70] B. Wang, R. Yan, H. Liu, Effects of Interactions between NiM (M = Mn, Fe, Co and Cu) Bimetals with MgO (100) on the Adsorption of CO_2, *Applied Surface Science*, Vol.258, No.22, 2012, pp. 8831-8836.

[71] H. W. Nesbitt, D. Banerjee, Interpretation of XPS Mn(2p) Spectra of Mn Oxyhydroxides and Constraints on the Mechanism of MnO_2 Precipitation, *American Mineralogist*, Vol.83, 1998, pp. 305-315.

[72] M. C. Biesinger, B. P. Payne, A. P. Grosvenor, L. W. M. Lau, A. R. Gerson, R. S. C. Smart, Resolving Surface Chemical States in XPS Analysis of First Row Transition Metals, Oxides and Hydroxides: Cr, Mn, Fe, Co and Ni, *Applied Surface Science*, Vol.257, 2011, pp. 2717-2730.

[73] O. A. Bulavchenko, Z. S. Vinokurov, T. N. Afonasenko, P. G. Tsyrul'nikov, S. V. Tsybulya, P. Dürre, Biobutanol: An Attractive Biofuel, *Biotechnology Journal*, Vol.2, No.12, 2007, pp. 1525-1534.

[74] J. M. Campos-Martín, J. L. G. Fierro, A. Guerrero-Ruiz, R. G. Herman, K. Klier, Promoter Effect of Cesium on C–C Bond Formation during Alcohol Synthesis from CO/H_2over $Cu/ZnO/Cr_2O_3$Catalysts, *Journal of Catalysis*, Vol.163, 1996, pp. 418-428.

[75] M. C. Biesinger, Advanced Analysis of Copper X-Ray Photoelectron Spectra, *Surface and Interface Analysis*, Vol.49, 2017, pp. 1325-1334.

[76] M. C. Biesinger, L. W. M. Lau, A. R. Gerson, R. C. Smart, Resolving Surface Chemical States in XPS Analysis of First Row Transition Metals, Oxides and Hydroxides: Sc, Ti, V, Cu and Zn, *Applied Surface Science*, Vol.257, 2010, pp. 887-898.

[77] A. Davidson, J. F. Tempere, M. Che, H. Roulet, G. Dufour, Spectroscopic Studies of Nickel(II) and Nickel(III) Species Generated upon Thermal Treatments of Nickel/Ceria-Supported Materials, *Journal of Physical Chemistry*, Vol.100, 1996, pp. 4919-4929.

[78] A. P. Grosvenor, M. C. Biesinger, R. C. Smart, N. S. McIntyre, New Interpretations of XPS Spectra of Nickel Metal and Oxides, *Surface Science*, Vol.600, 2006, pp. 1771-1779.

[79] A. C. Carreras, M. A. Cangiano, M. W. Ojeda, M. C. Ruiz, Characterization of Cu–Ni Nanostructured Alloys Obtained by a Chemical Route. Influence of the Complexing Agent Content in the Starting Solution, *Materials Characterization*, Vol.101, 2015, pp. 40-48.

[80] A. Kitla, O. V. Safonova, K. Föttinger, Infrared Studies on Bimetallic Copper/Nickel Catalysts Supported on Zirconia and Ceria/Zirconia, *Catalysis Letters*, Vol.143, 2013, pp. 517-530.

[81] B. C. Miranda, R. J. Chimentão, J. Szanyi, A. H. Braga, J. B. O. Santos, F. Gispert-Guirado, K. Barta, G. Bottari, Z. Sun, Supercritical Methanol as Solvent and Carbon Source in the Catalytic Conversion of 1,2-Diaminobenzenes and 2-Nitroanilines to Benzimidazoles, *Green Chemistry*, Vol.17, 2015, pp. 5172-5181.

[82] J. R. Rostrup-Nielsen, Making Fuels from Biomass, *Science*, Vol.308, 2005, pp. 1421–1422.

[83] J. Goldemberg, Ethanol for a Sustainable Energy Future, *Science*, Vol.315, 2007, pp. 808–810.

[84] M. Zhang, Y. Yu, Dehydration of Ethanol to Ethylene, *Industrial & Engineering Chemistry Research*, Vol.52, 2013, pp. 9505–9514.

[85] C. Angelici, B. M. Weckhuysen, P. C. A. Bruijnincx, Chemocatalytic Conversion of Ethanol into Butadiene and Other Bulk Chemicals, *ChemSusChem,* Vol.6, 2013, pp. 1595–1614.

[86] J. Lee, Y. Lee, S. Kim, E. E. Kwon, K.-Y. A. Lin, Catalytic Production of Hexamethylenediamine from Renewable Feedstocks, *Korean Journal of Chemical Engineering*, Vol.38, 2021, pp. 1079–1086.

[87] Statista, *Production of Bioethanol Worldwide in 2018*, by Region. Available online: https://www.statista.com/statistics/271471/bioethanol-production-in-selected-countries/ (accessed on 1 February 2026).

[88] S. Veibel, J. I. Nielsen, On the Mechanism of the Guerbet Reaction, *Tetrahedron*, Vol.23, 1967, pp. 1723–1733.

[89] E. Santacesaria, G. Carotenuto, R. Tesser, M. Di Serio, Ethanol Dehydrogenation to Ethyl Acetate by using Copper and Copper Chromite Catalysts, *Chemical Engineering Journal*, Vol.179, 2012, pp. 209–220.

[90] J. N. Chheda, J. A. Dumesic, An Overview of Dehydration, Aldol-Condensation and Hydrogenation Processes for Production of Liquid Alkanes from Biomass-Derived Carbohydrates, *Catalysis Today*, Vol.123, 2007, pp. 59–70.

[91] X.-Y. Xi, Z.-H. Sun, H.-T. Cao, Y.-T.; Pei, G. H. ten Brink, P. J. Deuss, K. Barta, H. J. Heeres, Catalyst Performance Studies on the Guerbet Reaction in a Continuous Flow Reactor Using Mono- and Bi-Metallic Cu-Ni Porous Metal Oxides, *Catalysts*, Vol.10, No.9, 2020, 996.

[92] R. L. Wingad, P. J. Gates, S. T. G. Street, D. F. Wass, Catalytic Conversion of Ethanol to n-

Butanol Using Ruthenium P–N Ligand Complexes, *ACS Catalysis*, Vol.5, 2015, pp. 5822–5826.

[93] K.-N. T. Tseng, S. Lin, J. W. Kampf, N. K. Szymczak, Upgrading Ethanol to 1-Butanol with a Homogeneous Air-Stable Ruthenium Catalyst, *Chemical Communications*, Vol.52, 2016, pp. 2901–2904.

[94] Y. Xie, Y. Ben-David, L. J. W. Shimon, D. Milstein, Highly Efficient Process for Production of Biofuel from Ethanol Catalyzed by Ruthenium Pincer Complexes, *Journal of the American Chemical Society*, Vol.138, 2016, pp. 9077–9080.

[95] H. Aitchison, R. L. Wingad, D. F. Wass, Homogeneous Ethanol to Butanol Catalysis—Guerbet Renewed, *ACS Catalysis*, Vol.6, 2016, pp. 7125–7132.

[96] C. N. Neumann, S. J. Rozeveld, M. Yu, A. J. Rieth, M. Dincă, Metal–Organic Framework-Derived Guerbet Catalyst Effectively Differentiates between Ethanol and Butanol, *Journal of the American Chemical Society*, Vol.141, 2019, pp. 17477–17481.

[97] D. J. Cole-Hamilton, Homogeneous Catalysis–New Approaches to Catalyst Separation, Recovery, and Recycling, *Science*, Vol.299, 2003, pp. 1702–1706.

[98] A. Dev, A. K. Srivastava, S. Karmakar, *New Generation Hybrid Nanobiocatalysts: The Catalysis Redefined*, In Handbook of Nanomaterials for Industrial Applications, C. Mustansar Hussain, Ed., Elsevier: Amsterdam, The Netherlands, pp. 217–231, 2018.

[99] C. R. Ho, S. Shylesh, A. T. Bell, Mechanism and Kinetics of Ethanol Coupling to Butanol over Hydroxyapatite, *ACS Catalysis*, Vol.6, 2016, pp. 939–948.

[100] D. Jiang, X. Wu, J. Mao, J. Ni, X. Li, Continuous Catalytic Upgrading of Ethanol to n-Butanol over Cu–CeO_2/AC Catalysts, *Chemical Communications*, Vol.52, 2016, pp. 13749–13752.

[101] X. Wu, G. Fang, Z. Liang, W. Leng, K. Xu, D. Jiang, J. Ni, X. Li, Catalytic Upgrading of Ethanol to n-Butanol over M-CeO_2/AC (M=Cu, Fe, Co, Ni and Pd) Catalysts, *Catalysis Communications*, Vol.100, 2017, pp. 15–18.

[102] D. Jiang, G. Fang, Y. Tong, X. Wu, Y. Wang, D. Hong, W. Leng, Z. Liang, P. Tu, L. Liu, K. Xu, J. Ni, X. Li, Multifunctional Pd@UiO-66 Catalysts for Continuous Catalytic Upgrading of Ethanol to n-Butanol, *ACS Catalysis*, Vol.8, No.12, 2018, pp. 11973–11978.

[103] T. Riittonen, K. Eränen, P. Mäki-Arvela, A. Shchukarev, A.-R. Rautio, K. Kordas, T. Tsuchida, J. Kubo, T. Yoshioka, S. Sakuma, T. Takeguchi, W. Ueda, Reaction of Ethanol over Hydroxyapatite Affected by Ca/P Ratio of Catalyst, *Journal of Catalysis*, Vol.259, No.2, 2008, pp. 183-189.

[104] M. Jones, C. Keir, C. Iulio, R. Robertson, C. Williams, D. Apperley, Investigations into the Conversion of Ethanol into 1,3-Butadiene, *Catalysis Science & Technology*, Vol.1, 2011, pp. 267-272.

[105] S. Hanspal, Z. D. Young, J. Tyler, P. Robert, J. Davis, Influence of Surface, Acid and Base Sites on the Guerbet Coupling of Ethanol to Butanol over Metal Phosphate Catalysts, *Journal of Catalysis*, Vol.352, 2017, pp. 182-190.

[106] M. C. Abelló, M. F. Gómez, L. A. Arima, Synthesis of 1,1-Diethoxyethane from Bioethanol. Influence of Catalysts Acidity, *Reaction Kinetics & Catalysis Letters*, Vol.73, 2001, pp. 143-149.

[107] M. Almohalla, E. Gallegos-Suarez, A. Arcoya, I. Rodríguez-Ramos, A. Guerrero-Ruiz, Comparative study of bioethanol transformation catalyzed by Ru or Pt nanoparticles supported on KL zeolite, *Catalysis Science & Technology*, Vol.6, No.2, 2016, pp. 521-529.

[108] T. Riittonen, E. Toukoniitty, D. K. Madnani, A.-R. Leino, K. Kordas, M. Szabo, A. Sapi, K. Arve, J. Wärnå, J.-P. Mikkola, One-Pot Liquid-Phase Catalytic Conversion of Ethanol to 1-Butanol over Aluminium Oxide—The Effect of the Active Metal on the Selectivity, *Catalysts*, Vol.2, 2012, pp. 68–84.

[109] C. D. Chang, A. J. Silvestri, The Conversion of Methanol and Other O-Compounds to Hydrocarbons over Zeolite Catalysts, *Journal of Catalysis*, Vol.47, No.2, 1977, pp. 249-259.

[110] C. E. O. Rojas, *Dimethyl Ether as Building Block for the Production of Green Fuels*, Ph.D. thesis from Eindhoven University of Technology, 2018.

[111] M. Keraron, *Conversion of Methanol to Olefins on SAPO-34: Kinetic Modelling and Reactor Design*, Ecole Polytechnique, Montreal (Canada), Master of Thesis, 192 pages, 2010.

APPENDIX

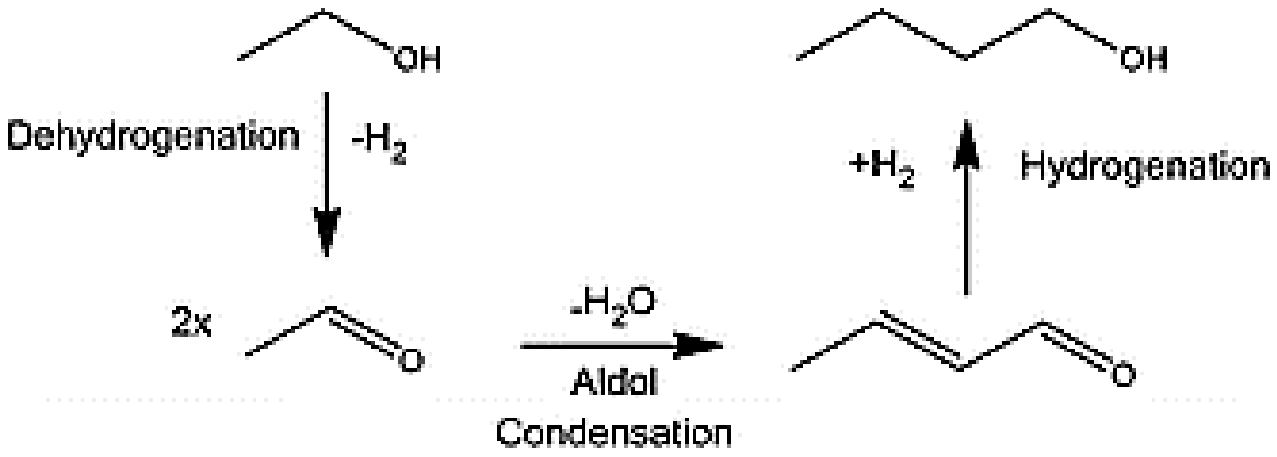

Figure 1. The Guerbet reaction: dehydrogenation of ethanol to acetaldehyde, followed by aldol condensation of acetaldehyde to form crotonaldehyde; Finally, butanol is formed *via* hydrogenation of crotonaldehyde.

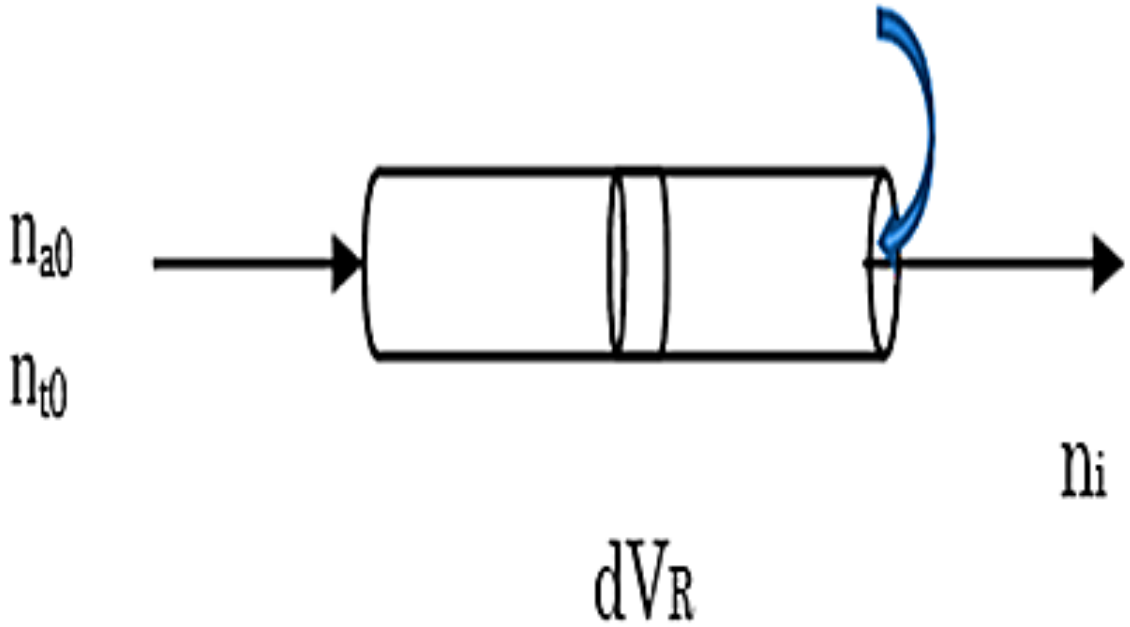

Figure 2. Representation of the PFR.

Table 1. Calorific capacities, enthalpies and free energies of compounds formation involved in the synthesis of dimethyl ether.

Compounds	**ΔH^o (kj/mol) at 25°C**	**ΔG^o (kj/mol) at 25°C**	**C_p (J/mol.°C)**	**ΔH^o reaction (kj/mol)**	**ΔG^o Reaction (kJ/mol)**
CH_3OH	- 201.54	- 166.51	79.5		
CH_3OCH_3	- 184.05	- 112.93	64.4	- 22.27	- 8.51
H_2O (Gaseous)	- 241.80	- 228.60	33.6		

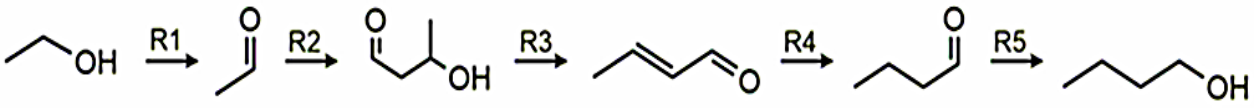

Figure 3. The Guerbet reaction mechanism steps.

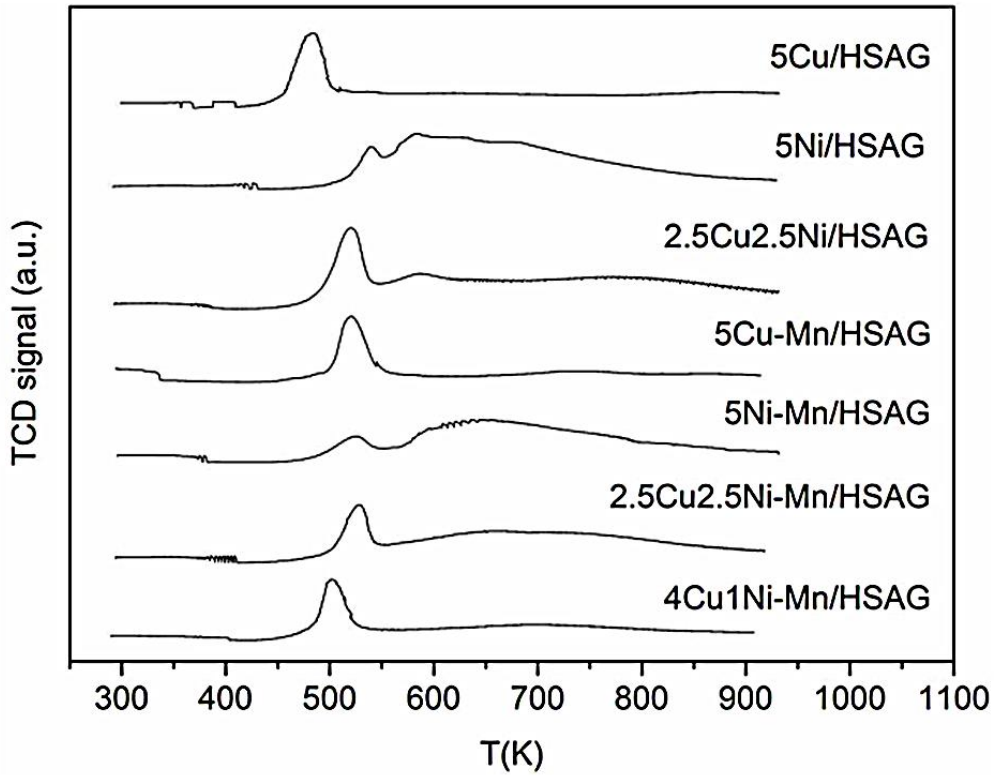

Figure 4. H_2-TPR profiles of the catalyst's samples.

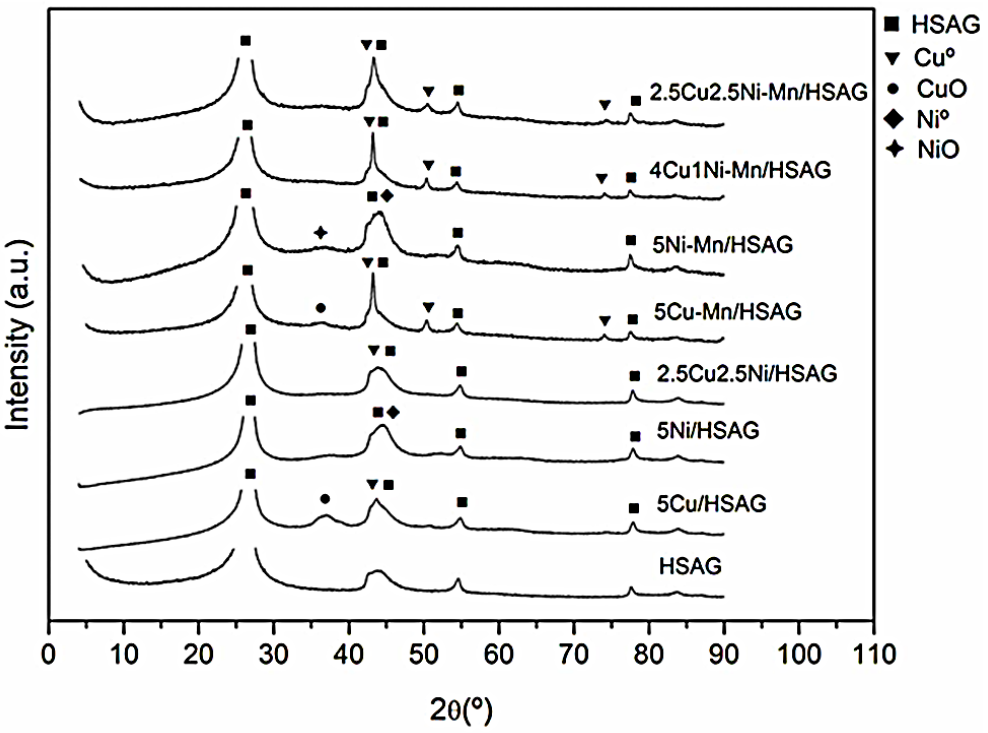

Figure 5. XRD patterns of the support HSAG and the reduced catalysts.

Table 2. Support and reduced catalysts textural parameters

Samples	**S_{BET} (m^2/g)**	**Desorption Pore volume [a] (cm^3/g)**
HSAG	400	0.52
Mn/HSAG	322	-
5Cu-Mn/HSAG	235	-
5Ni-Mn/HSAG	280	-
2.5Cu2.5Ni-Mn/HSAG	231	0.24
[a] : BJH desorption pore volume		

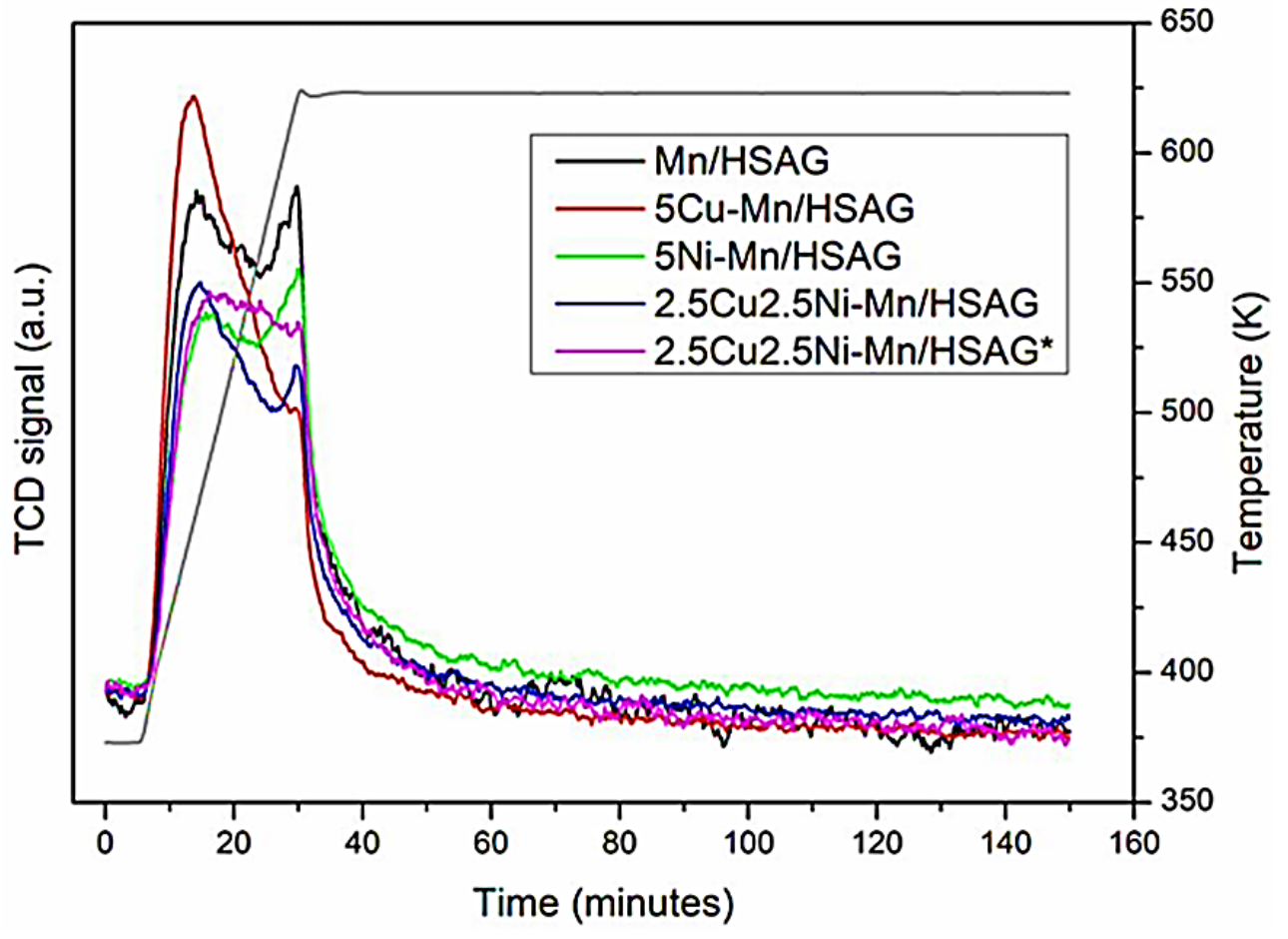

Figure 6. NH_3-TPD profiles of the bifunctional catalysts reduced in situ. * Thermally treated in He(g) at 450°C prior reduction with H_2(g).

Table 3. Acidity distribution derived after deconvolution of the NH_3-TPD profiles of the Cu-Ni-Mn NCs reduced in situ.

Samples	NH_3-TPD Area (a.u.)	Acid Sites (%)		
		Weak (%)	Medium (%)	Strong (%)
Mn/HSAG	2.5	40	25	36
5Cu-Mn/HSAG	2.1	53	26	24
5Ni-Mn/HSAG	2.0	36	28	40
2.5Cu2.5Ni-Mn/HSAG	2.1	47	22	35
2.5Cu2.5Ni-Mn/HSAG [a]	2.3	41	34	38
[a] : Thermally treated in He(g) at 450°C before reduction with H_2.				

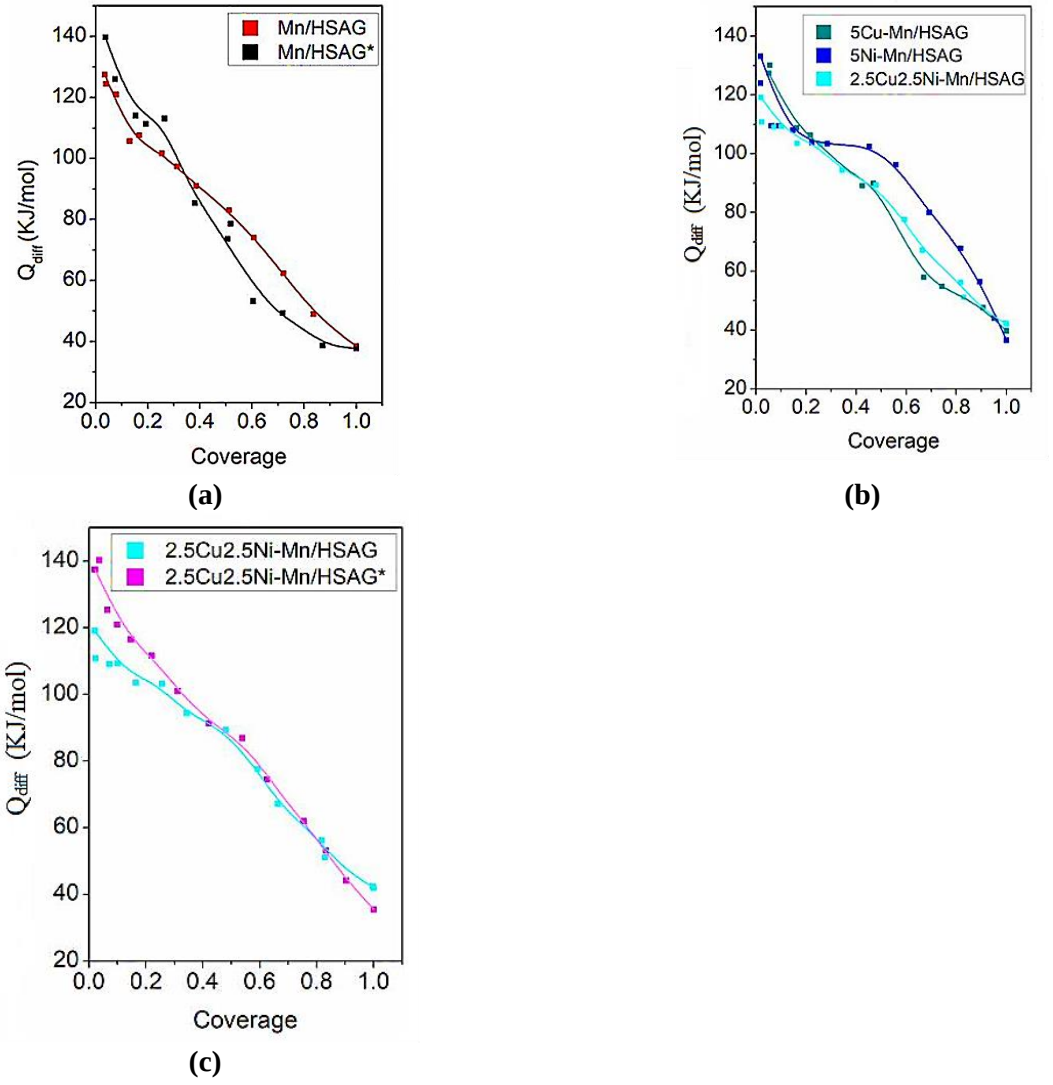

Figure 7. Differential heats of CO_2 adsorption vs. coverage at 50°C; **(a)** Mn/HSAG before and after thermal treatment, **(b)** Cu-Ni bifunctional catalysts, and **(c)** 2.5Cu2.5Ni Mn/HSAG before and after thermal treatment. * Thermally treated in He(g) at 450°C prior reduction with H_2.

Table 4. CO_2 chemisorption capacities at 50ºC and type of basic sites distribution.

Samples	**Total µmol CO_2/g** [a]	**Basic Sites (%)**		
		Strong (%) [b]	**Medium (%)** [c]	**Weak (%)** [d]
Mn/HSAG	40	43	34	24
Mn/HSAG [e]	42	42	26	32
5Cu-Mn/HSAG	22	45	22	30
5Ni-Mn/HSAG	51	62	27	13
2.5Cu2.5Ni-Mn/HSAG	56	42	32	24
2.5Cu2.5Ni-Mn/HSAG [e]	58	50	35	20

a: (Q_{diff} > 40 kJ/mol)
b: (Q_{diff} >90 kJ/mol)
c: (90 > Q_{diff} > 60 kJ/mol)
d: (60 > Q_{diff} > 40 kJ/mol)
e: Thermally treated in He(g) at 450ºC before reduction with H_2
pH=8.02, after 15 min

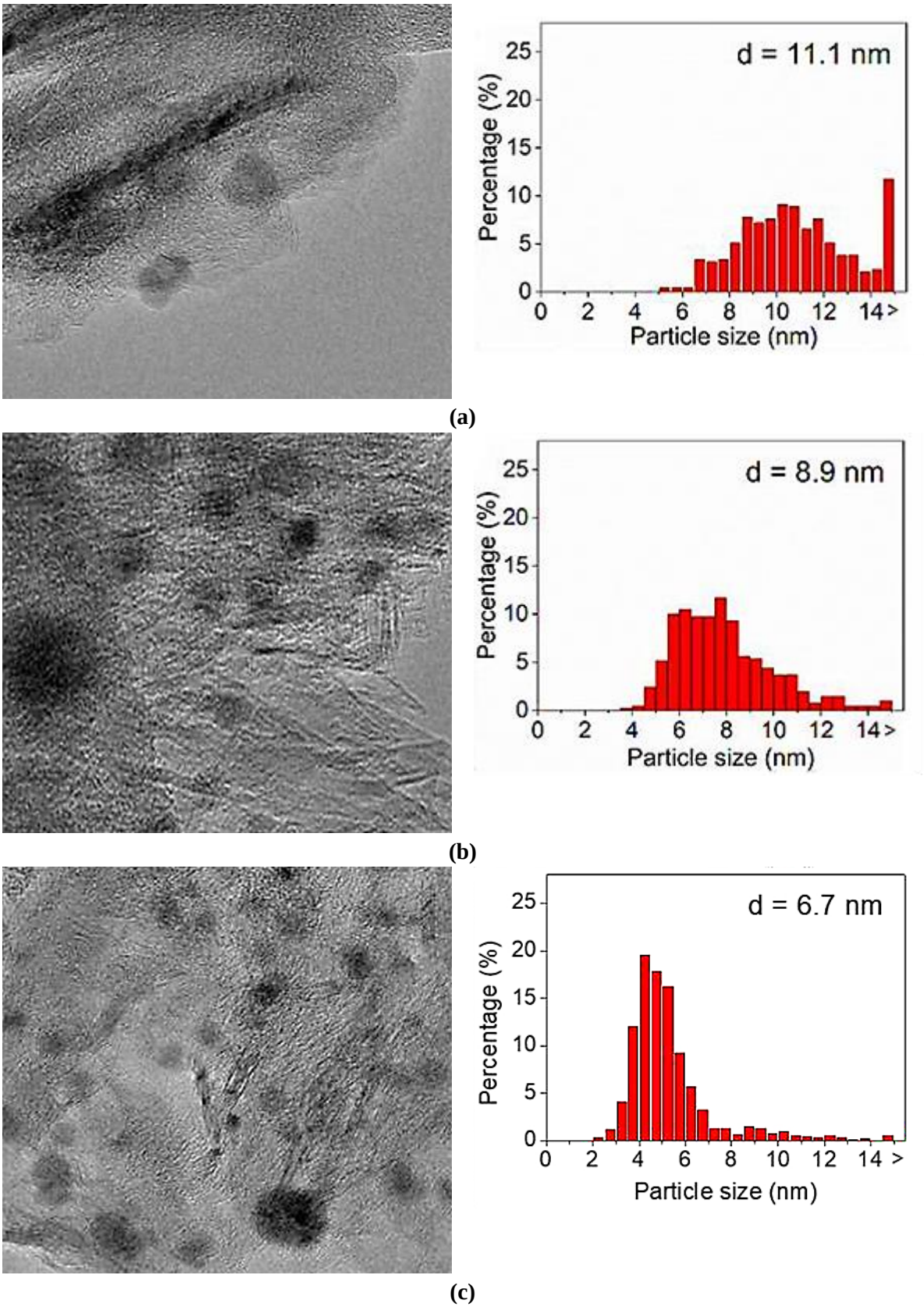

Figure 8. TEM images of catalysts after reaction; **a)** 5Cu/HSAG (d = 11.1 nm), **b)** 5Ni/HSAG (d = 8.9 nm) and **c)** 2.5Cu2.5Ni/HSAG (d = 6.7 nm).

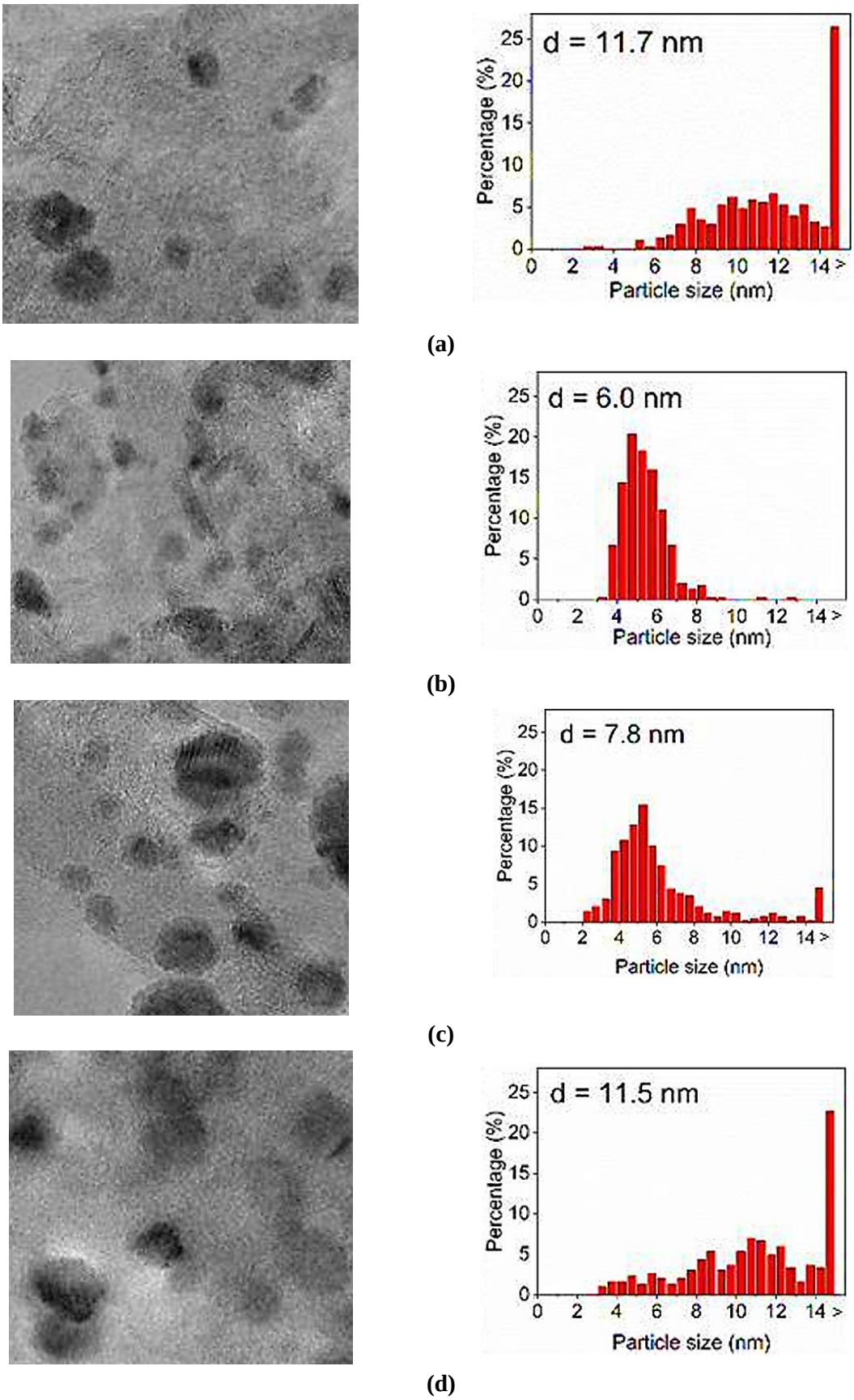

Figure 9. TEM images of catalysts after reaction: **a)** 5Cu-Mn/HSAG (d = 11.7 nm), **b)** 5Ni-Mn/HSAG (d = 6.0 nm), **c)** 2.5Cu2.5Ni-Mn/HSAG (d = 7.8 nm), **d)** 2.5Cu2.5Ni-Mn/HSAG (d = 11.5 nm), (Thermally treated in He(g) at 450ºC with H_2).

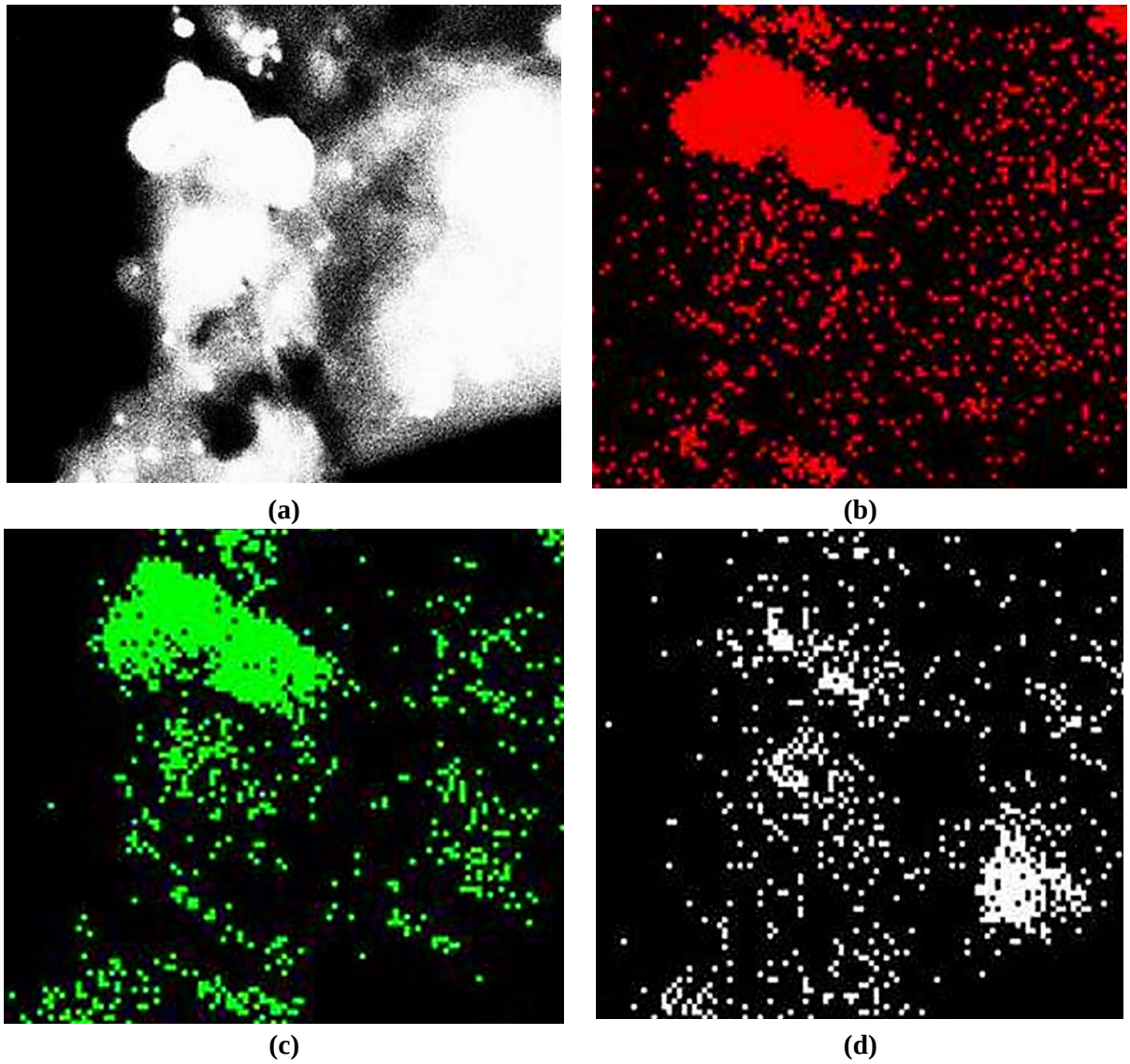

Figure 10. EDX elemental mapping of 2.5Cu2.5Ni-Mn/HSAG; **a)** reduced in H_2 at 300ºC, **b)** Cu after reaction, **c)** Ni after reaction and **d)** Mn after reaction, respectively.

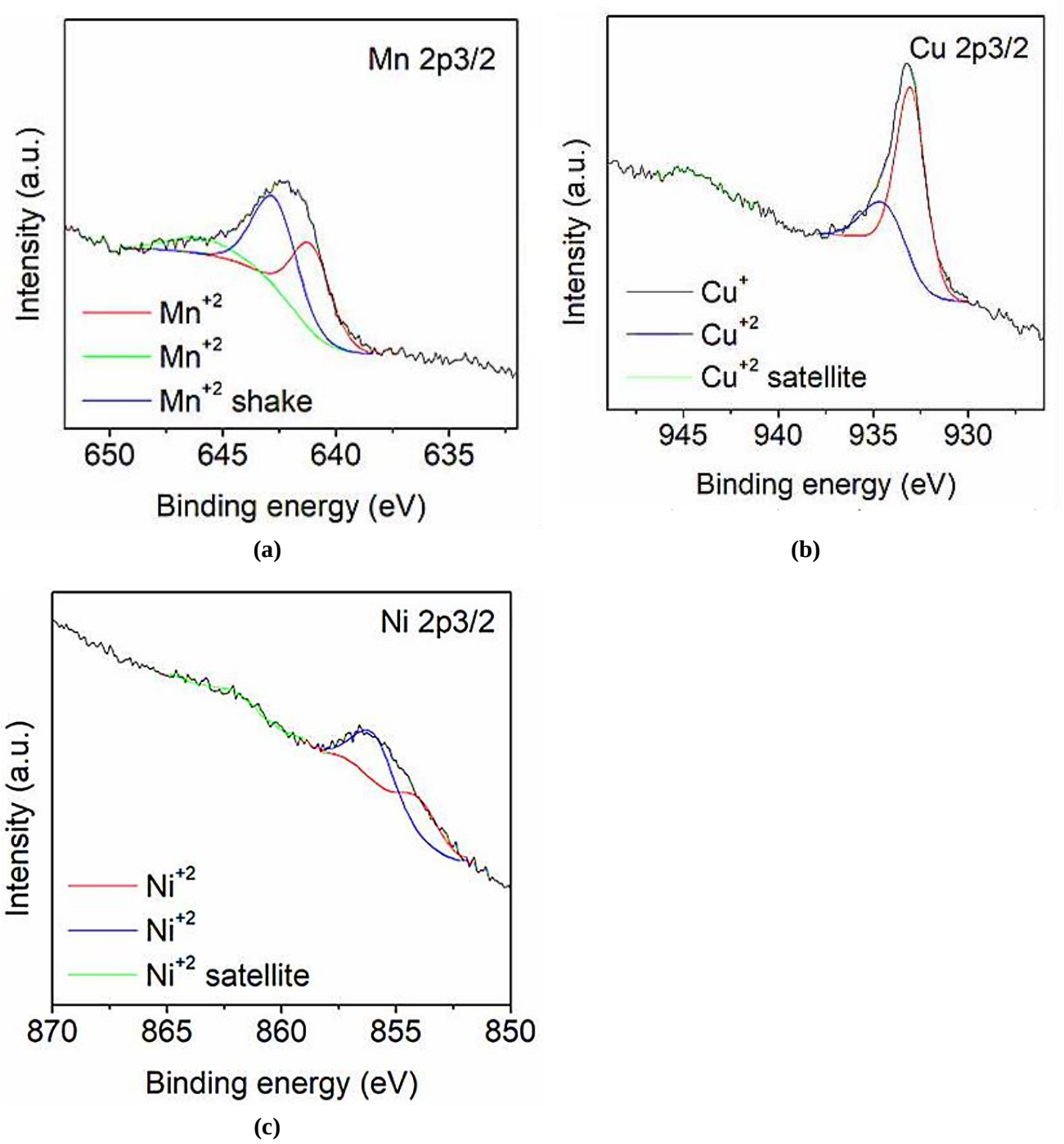

Figure 11. XPS spectra of 2.5Cu2.5Ni-Mn/HSAG sample; **a)** Mn $2p_{3/2}$, **b)** Cu $2p_{3/2}$ and **c)** Ni $2p_{3/2}$, (2.5Cu2.5Ni-Mn/HSAG sample reduced in H_2 at 300°C).

Table 5. Binding energies (eV) of core electrons and the Auger parameter (eV) of nanocomposite samples reduced in H_2 at 300ºC and after reaction (R).

Samples	BE (eV)							Auger param. (eV)
	Cu 2p 3/2		Ni 2p 3/2		Mn 2p 3/2			
	Cu^{+}	Cu^{+2}	Ni^{+2}	Ni^{+2}	Mn^{+2}	Mn^{+2}	Mn^{+2} shake	
5Cu-Mn/HSAG	932.1	932.2	-	-	641.2	644.3	646.7	1849.9
5Ni-Mn/HSAG	-	-	853.1	855.2	641.0	644.4	644.1	-
2.5Cu2.5Ni-Mn/HSAG	932.3	932.7	853.4	855.3	641.5	644.8	646.2	1849.2
R-5Cu-Mn/HSAG	932.5	932.0	-	-	641.7	644.0	646.6	1849.7
R-5Ni-Mn/HSAG	-	-	853.6	855.9	641.3	644.9	646.3	-
R-2.5Cu2.5Ni-Mn/HSAG	932.8	-	853.3	856.2	641.9	645.1	646.8	1849.6

Table 6. Atomic ratios for catalysts samples reduced in H_2 at 300ºC and after reaction (R).

Samples	Cu/C	Ni/C	Mn/C	Cu/Ni	Cu/Mn	Ni/Mn
5Cu-Mn/HSAG	0.0014	-	0.0012	-	1.17	-
5Ni-Mn/HSAG	-	0.0005	0.0013	-	-	0.34
2.5Cu2.5Ni-Mn/HSAG	0.0007	0.0004	0.0012	2.29	0.48	0.22
R-5Cu-Mn/HSAG	0.0011	-	0.0010	-	0.96	-
R-5Ni-Mn/HSAG	-	0.0003	0.0008	-	-	0.27
R-2.5Cu2.5Ni-Mn/HSAG	0.0003	0.0002	0.0009	1.48	0.27	0.18

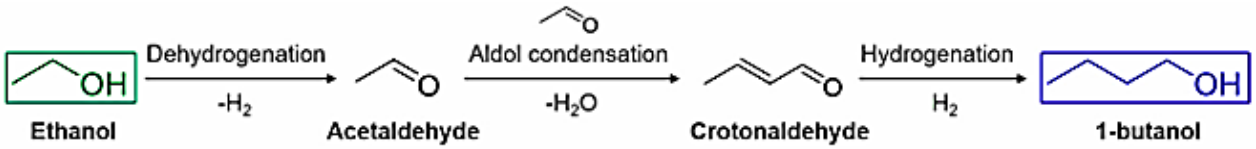

Figure 12. Representative reaction pathway for the conversion of ethanol to n-butanol via aldol condensation, [85].

Table 7. Catalytic activity and product selectivity for 1-butanol production from ethanol with Cu-Ni-Mn NCs, at 230°C and at 49.4 atm and at pH=8.02 after 15 min on stream.

Sample	d (nm) [a]		Selectivity (%)						Conv.
	Fresh	Used	ButOH	CO	CH_4	Ac	DEE	Others [b]	(%)
Cu/HSAG	4.6	11.3	6	0	0	55	33	14	18
Ni/HSAG	4.8	8.6	11	17	27	27	4	29	25
Mn/HSAG	-	-	0	0	0	4	0	43	0.2
2.5Cu2.5Ni/HSAG	3.7	6.9	8	13	16	41	7	24	21
5Cu-Mn/HSAG	8.1	11.9	34	0	0	28	16	27	52
5Ni-Mn/HSAG	5.2	6.1	27	11	24	12	3	34	59
4Cu1Ni-Mn/HSAG	5.4	8.4	39	8	9	19	10	29	38
2.5Cu2.5Ni-Mn/HSAG	7.7	7.5	95	9	12	15	5	32	61
2.5Cu2.5Ni-Mn/HSAG [c]	7.5	11.7	96	6	7	21	6	28	62

ButOH: 1-Butanol.
Ac: Acetaldehyde,
DEE: 1,1-diethoxy ethane,
a: Average particle size (nm) measured by TEM of fresh catalysts reduced at 300°C, except Ni/HSAG and 5Ni-Mn/HSAG that were reduced at 450°C and after 24 h in reaction.
b: Other products: diethyl ether, ethyl acetate, 2-butanona, diethoxy butane, 1-octanol, butanal, 2-butenal, 2-butanol, 2-ethyl-1-butanol, 1-octanol, 2-ethyl-1-hexanol, ethylene, ethane, acetone, propane, pentane.
c: After thermal treatment in Helium at 450°C before reduction with H_2.

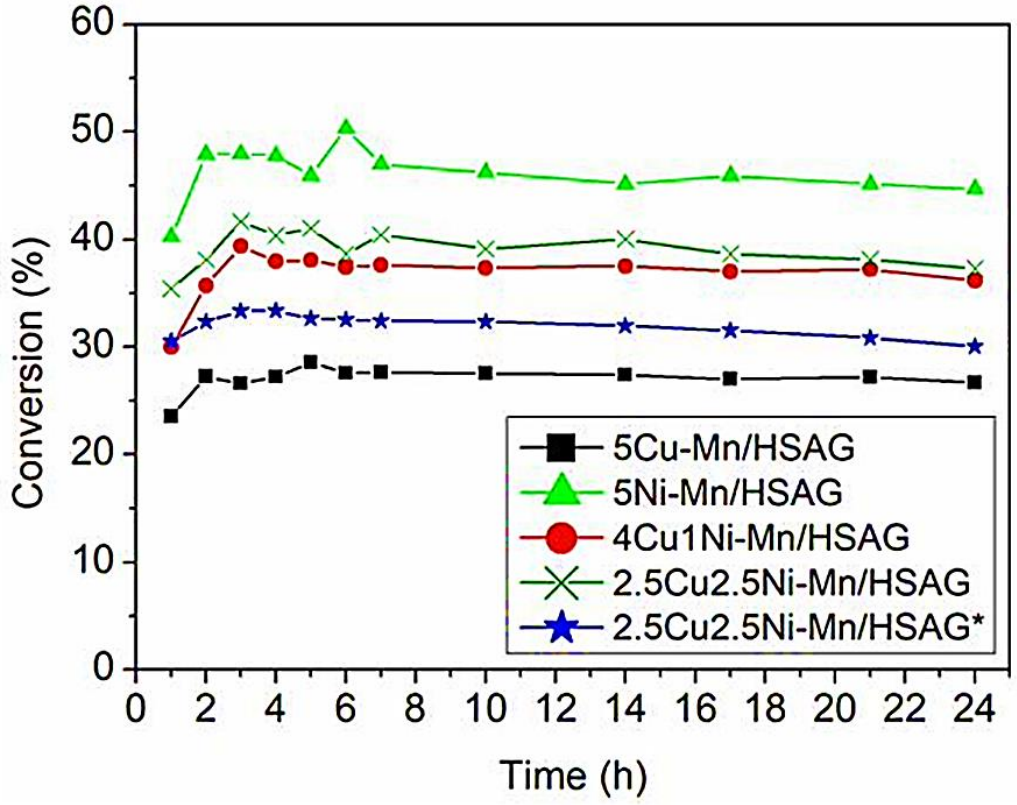

(a)

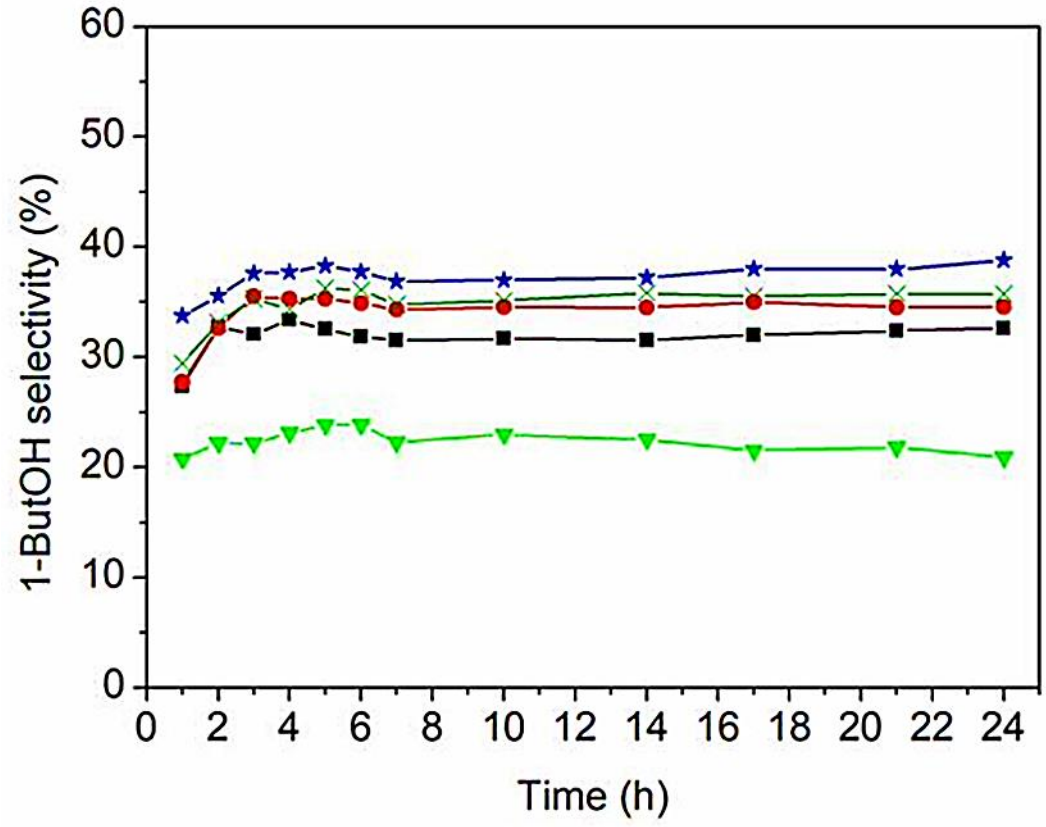

(b)

Figure 13. (a) Conversion and **(b)** 1-butanol selectivity through 24 h of reaction. * After thermal treatment in helium at 450°C prior reduction with H_2.

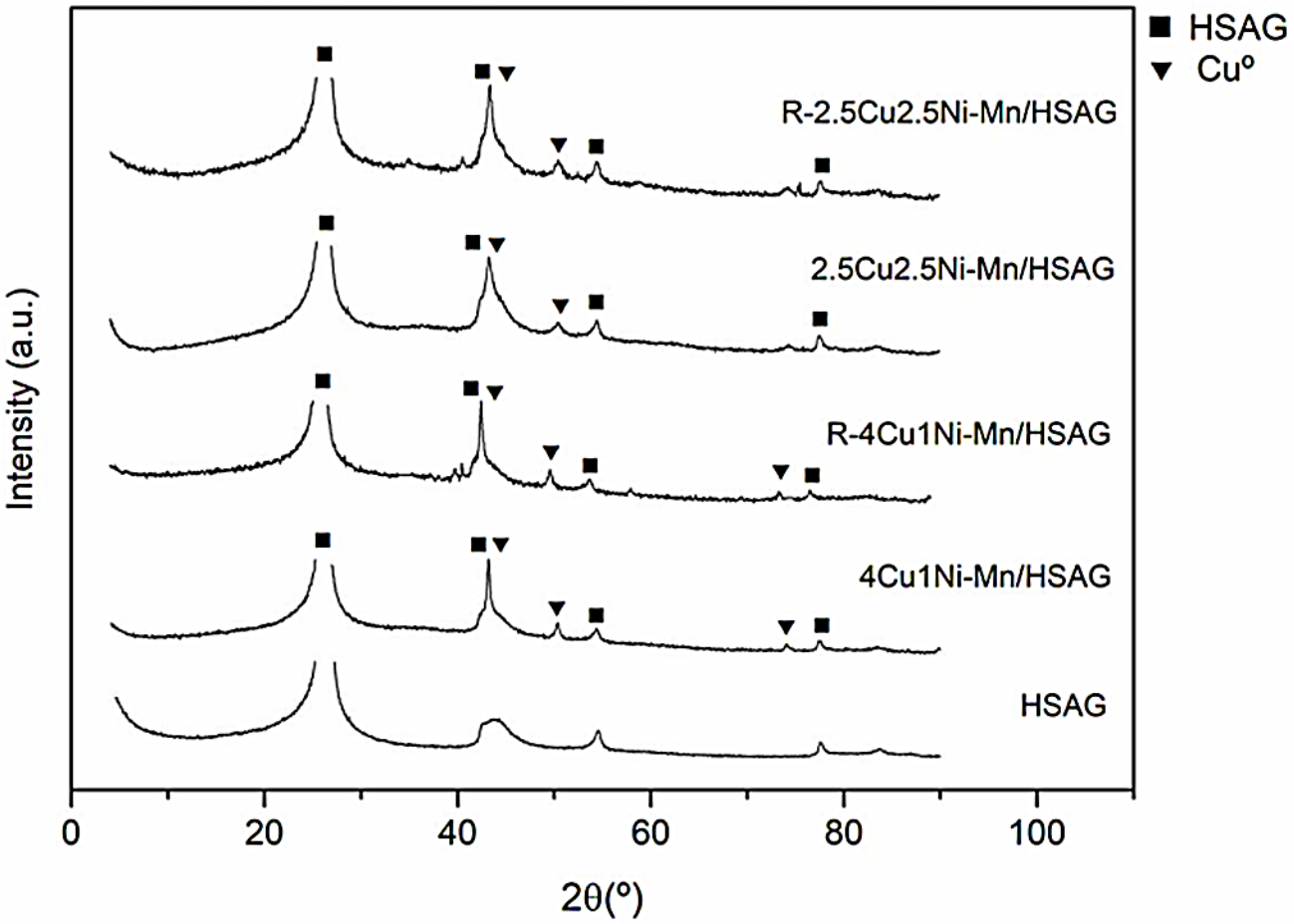

Figure 14. XRD patterns of the support HSAG and the catalysts 4Cu1Ni-Mn/HSAG and 2.5Cu2.5Ni-Mn/HSAG, both reduced at 300ºC with H_2, and after study in reaction (R-).

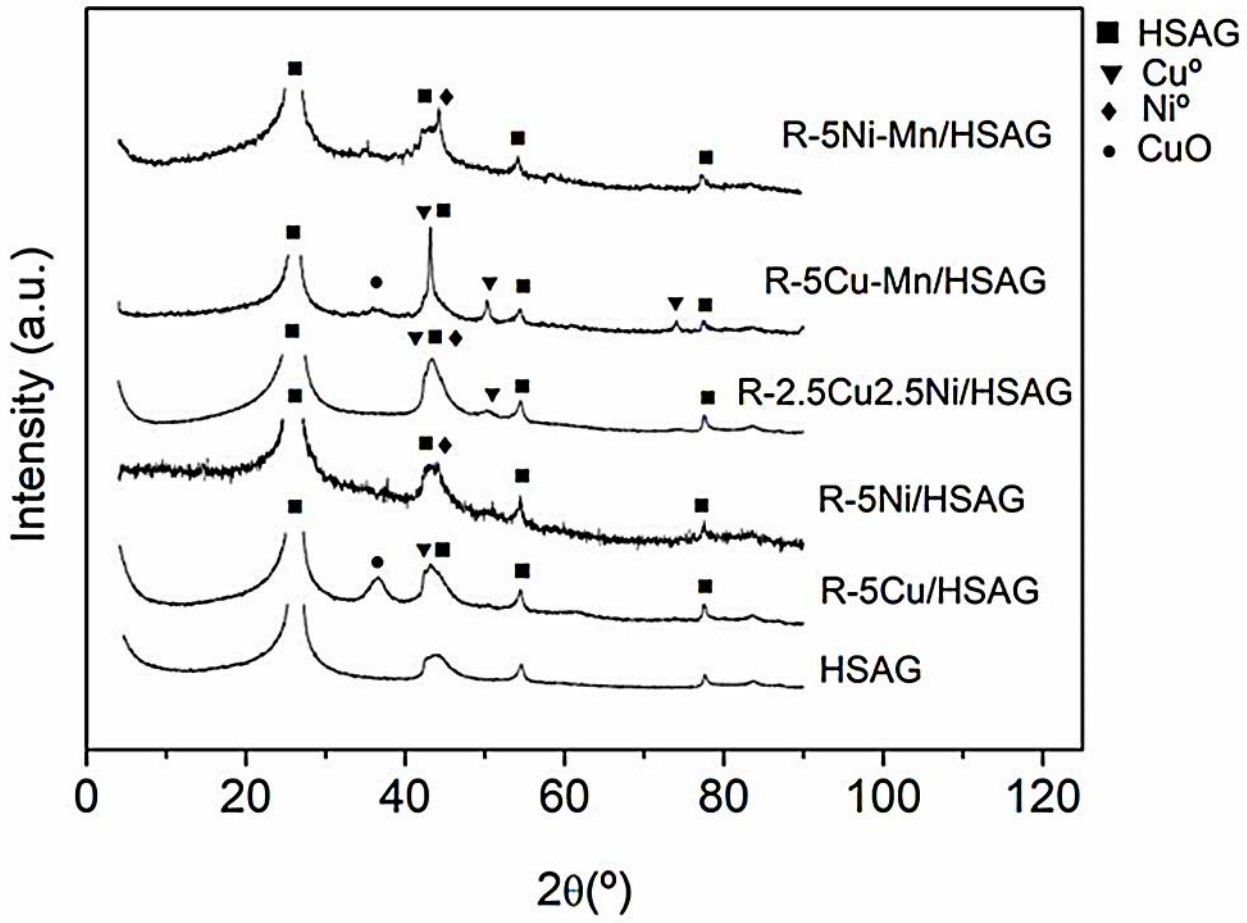

Figure 15. XRD patterns of the support HSAG and the catalysts after reaction (R).

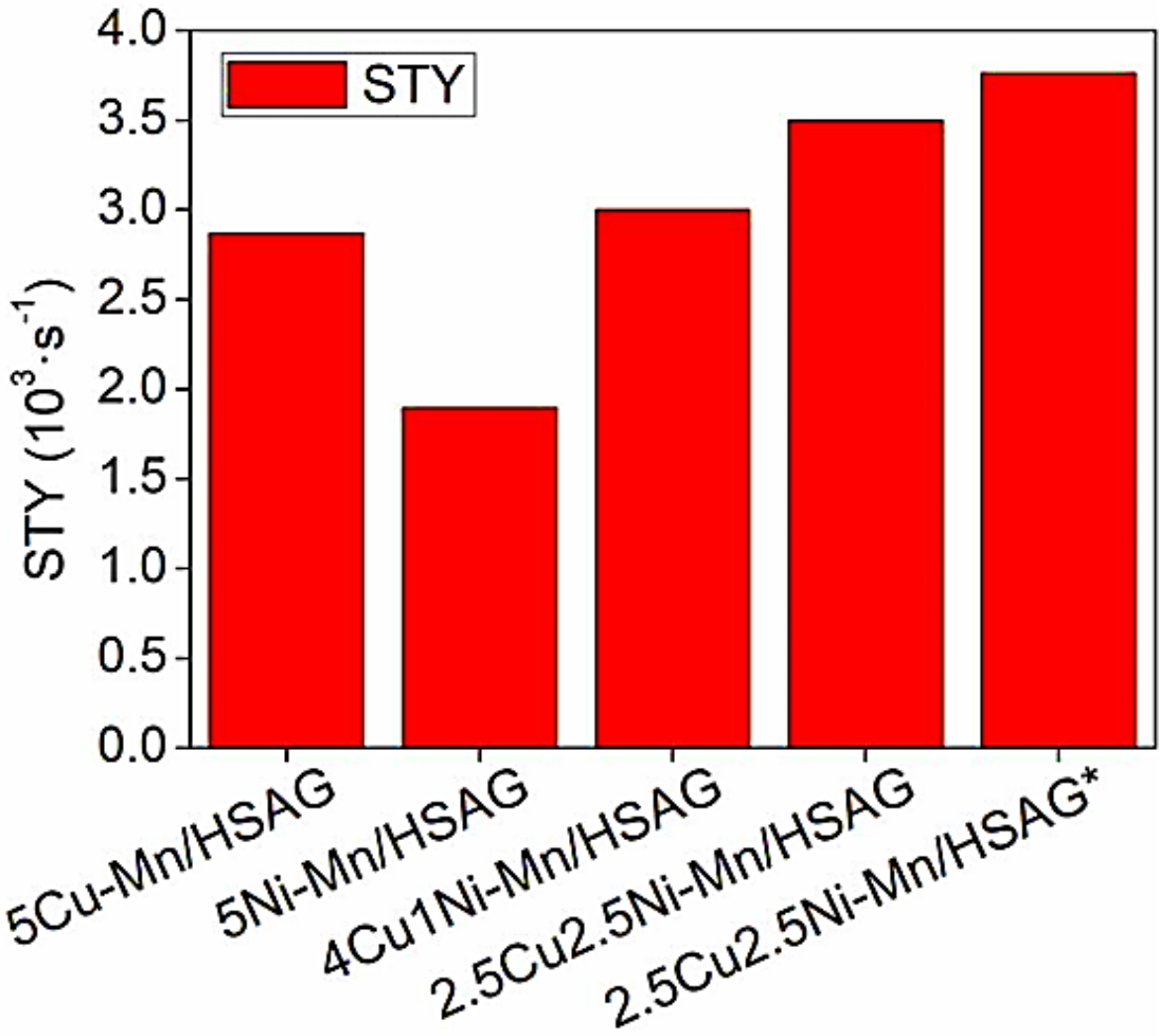

Figure 16. Site time yield (STY) (1/s) for the different Cu-Ni-Mn NCs samples after 7 h reaction.

Table 8. Leaching tests during catalyst recycling for Cu-Ni-Mn NCs catalyst.

Cycles	Cu (mg/l) [a]	Ni (mg/l)	Mn (mg/l)
1	0.6	0.3	9.0
2	0.6	0.3	8.0
3	0.5	0.3	8.0
4	0.5	0.3	7.0
5	0.5	0.2	6.0
6	0.4	0.2	5.0
7	0.4	0.1	4.0
8	0.3	0.1	2.0
9	0.2	0.1	1.0
[a] : Concentration is based on the solution after diluted by THF to 10 ml volume.			

Table 9. Catalytic performance after 24 h on reaction at 230°C and 48.36 atm, conversion and selectivity (WHSV in ethanol was 1.9 h^{-1}), and average particle sizes of the catalysts obtained by TEM.

Catalyst	Selectivity (%)								
	Conv. (%)	ButOH	Ac	CO	CH_4	1,1-DEE	Others	d (nm) [a]	d (nm) [b]
Cu/HSAG	17	4	52	0	0	31	13	4.7	11.1
Ni/HSAG	23	7	24	15	25	1	28	4.9	8.9
4Cu-1Ni/HSAG	20	5	39	8	12	13	23	4.2	7.1
5Cu-Mn/HSAG	26	26	23	0	0	15	36	7.5	8.9
5Ni-Mn/HSAG	23	24	12	15	25	2	22	4.5	5.5
2.5Cu2.5Ni-Mn/HSAG	28	32	13	11	15	2	27	5.8	9.3
4Cu1Ni-Mn/HSAG	24	39	22	4	6	4	25	6.6	7.1
4.75Cu0.25Ni-Mn/HSAG	28	31	23	2	2	10	32	6.8	8.5
4Cu1Ni-Mn/HSAG*	20	44	21	3	2	3	27	8.8	9.7
ButOH: 1-butanol, Ac: acetaldehyde, 1,1-DEE: 1,1-diethoxy ethane, d(nm): TEM average particle size of freshly reduced catalysts ([a]), and after 24 h in reaction ([b]). * Catalyst treated at 450°C in He(g) atmosphere prior in situ reduction.									

Figure 17. Block diagram.

Table 10. Tables od different temperatures for the operation of the PFR reactor.

Chemical Reaction	$2CH_3OH \rightarrow CH_3OCH_3 + H_2O$
ΔH^o RX (kj/mol)	-22.77
ΔG^o RX (kj/mol)	-8.51
k_0	1.00
T(^{o}K)	K_{eq}
250-650	1.00
650-1000	1.00
350-1000	0.99

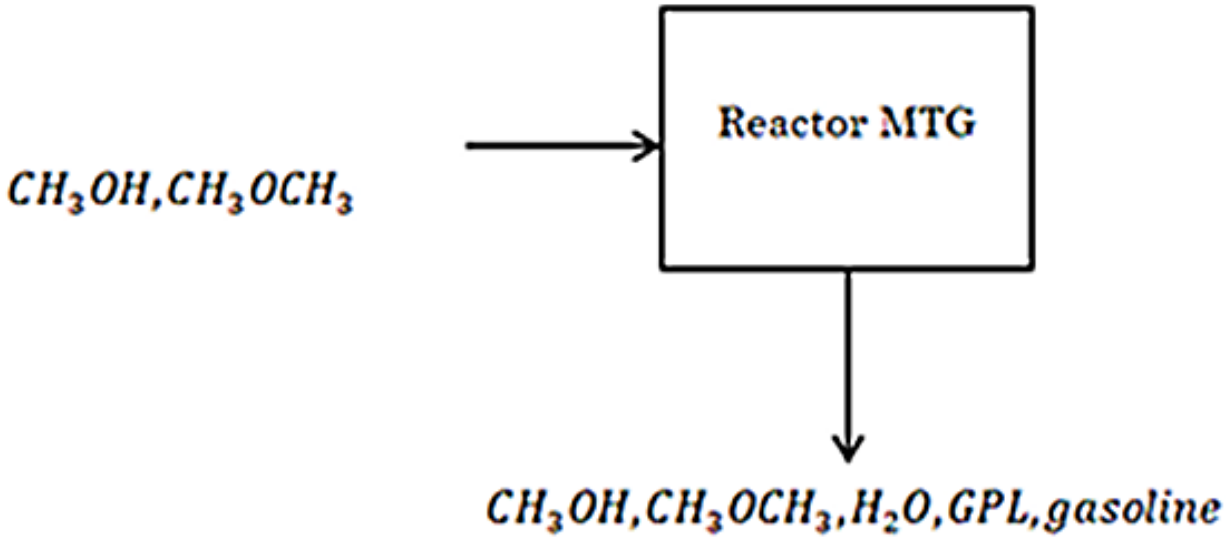

Figure 18. MTG process block diagram.

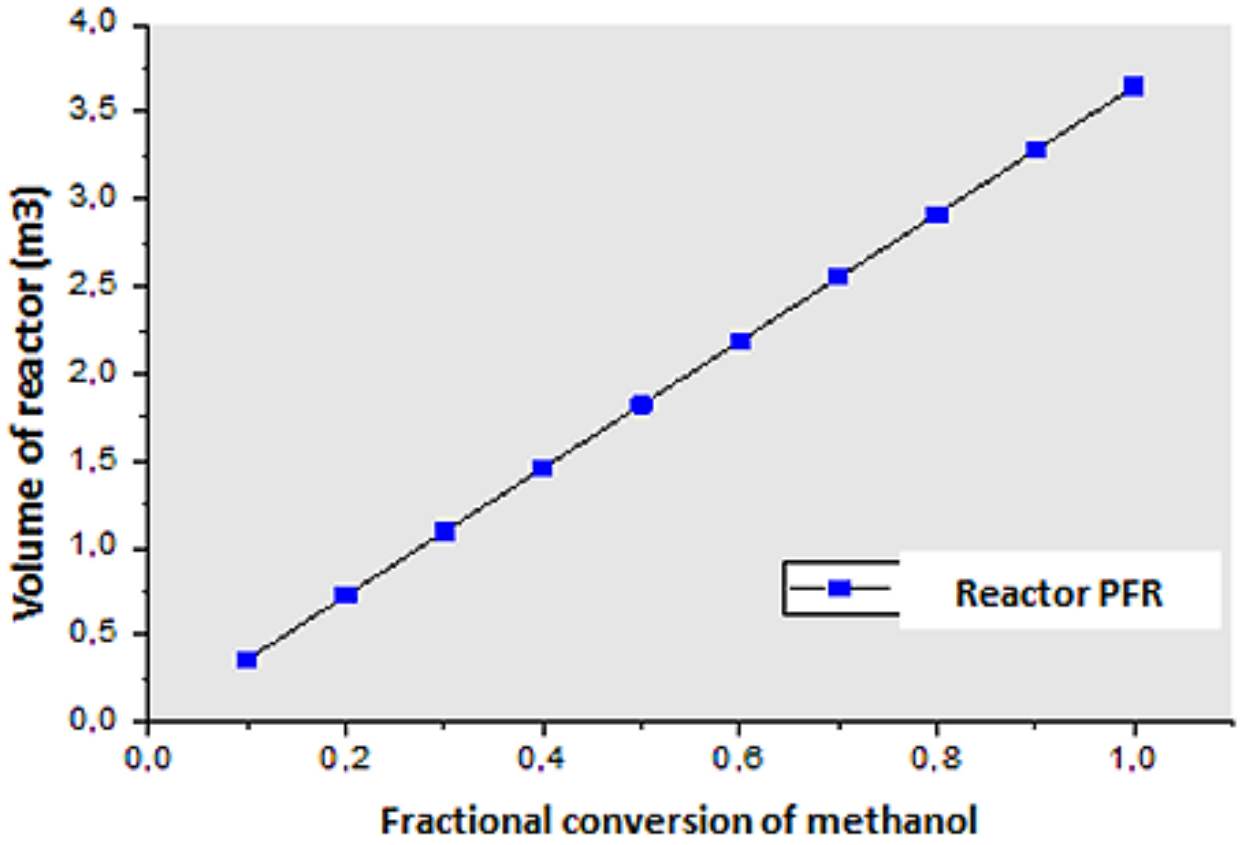

Figure 19. Graph showing the effect of the fractional conversion of methanol on the volume of the PFR reactor.

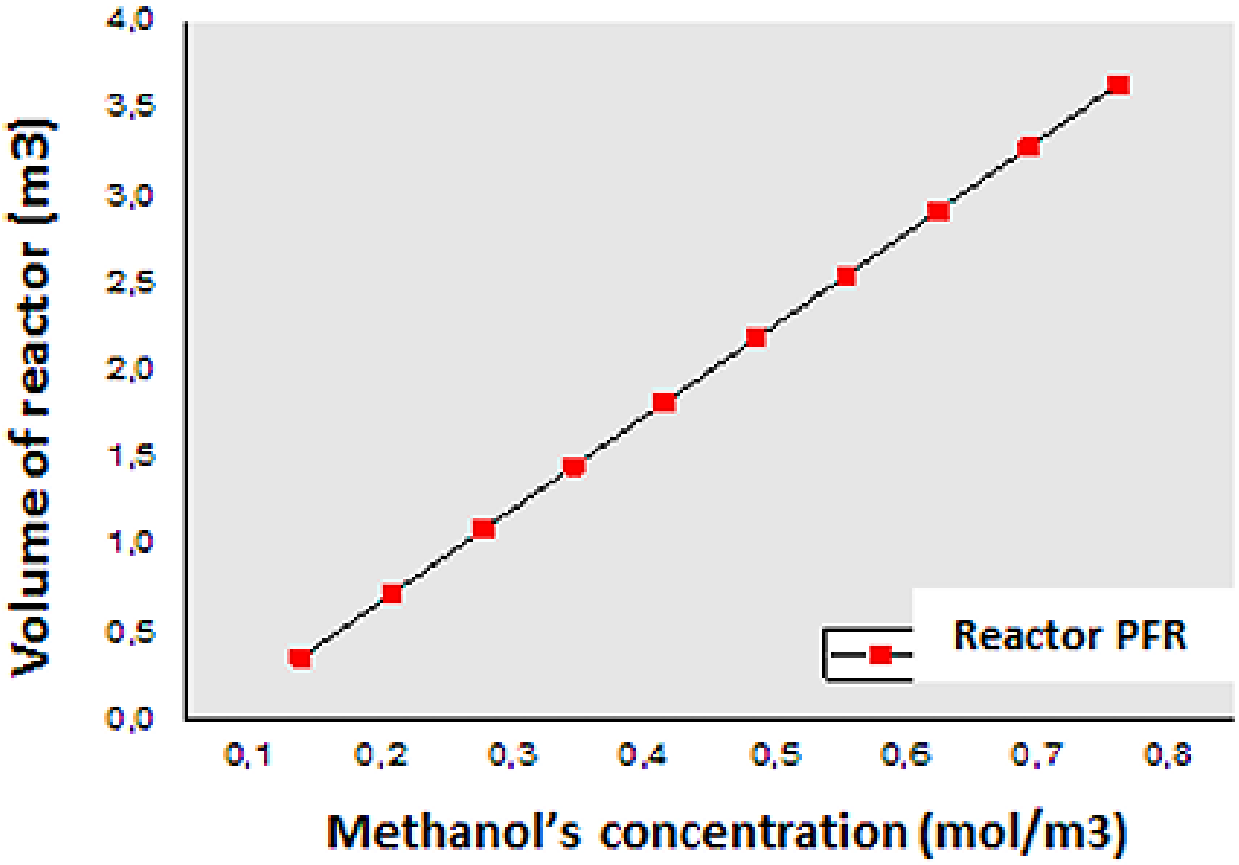

Figure 20. Graph showing the effect of the concentration of methanol on the volume of the PFR reactor.

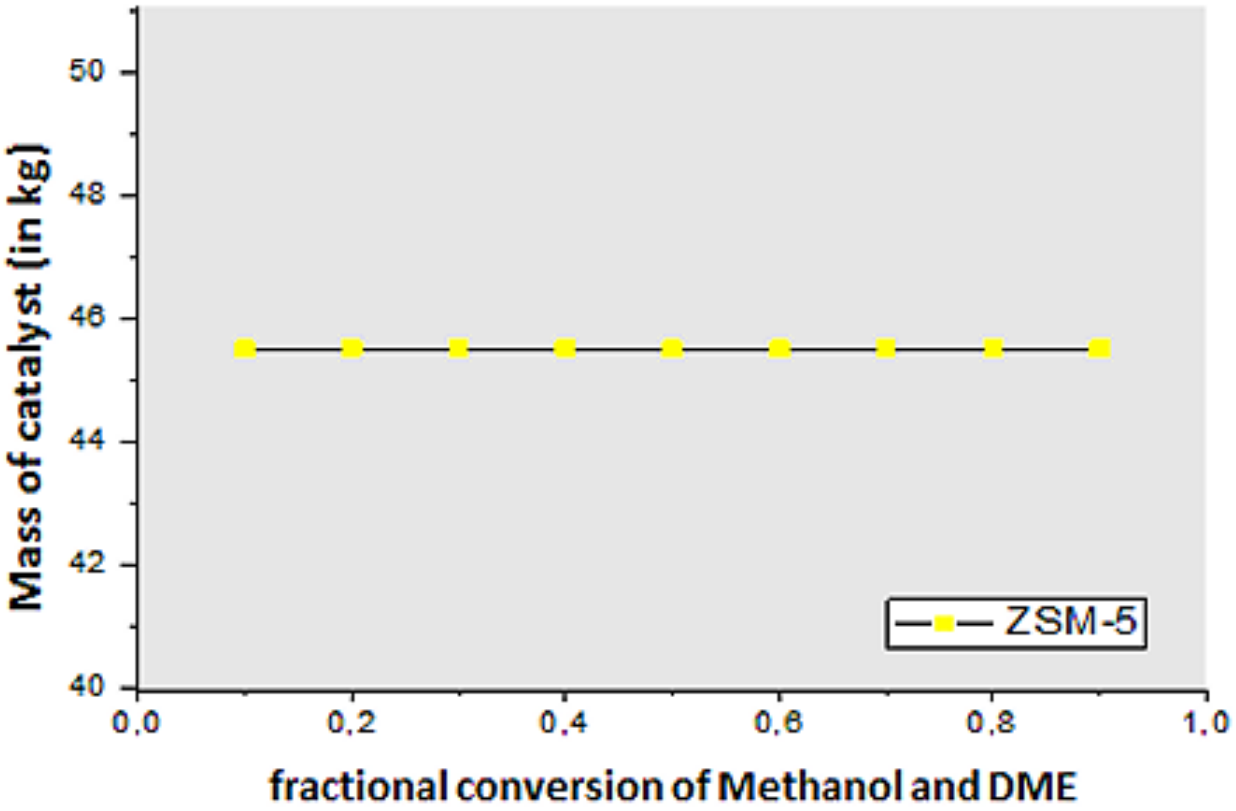

Figure 21. Graph showing the mass of the catalyst as a function of the conversion of dimethyl ether and methanol.

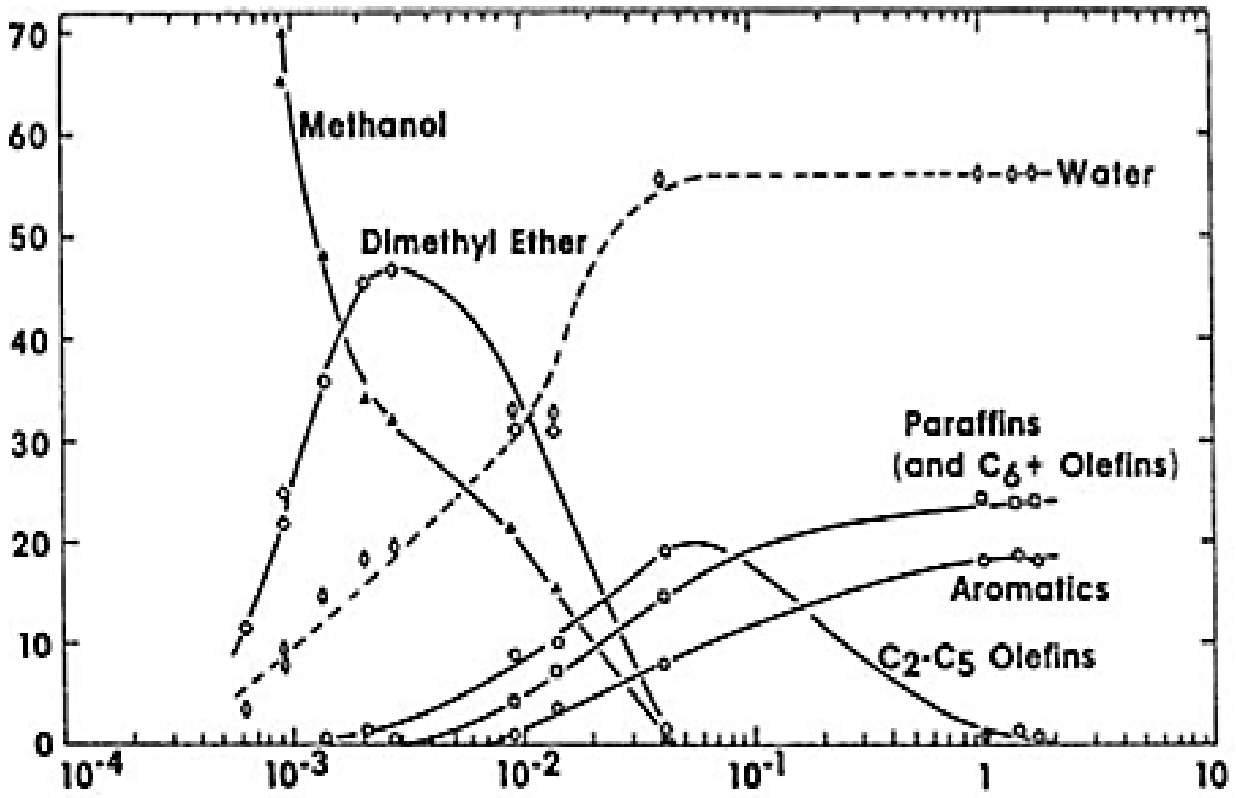

Figure 22. Fractional conversion of methanol to hydrocarbons by residence time on H-ZSM-5, [].